The Journal of Chemical Physics

Complete characterization of the 3p Rydberg complex of a molecular ion: $MgAr^+$. I. Observation of the $Mg(3p_\sigma)Ar^+$ B^+ state and determination of its structure and dynamics

Cite as: J. Chem. Phys. **153**, 074310 (2020); https://doi.org/10.1063/5.0015603
Submitted: 29 May 2020 . Accepted: 19 July 2020 . Published Online: 20 August 2020

Dominik Wehrli, Matthieu Génévriez, Stefan Knecht, Markus Reiher, and Frédéric Merkt

AIP Publishing

The Journal of Chemical Physics ARTICLE scitation.org/journal/jcp

Complete characterization of the 3p Rydberg complex of a molecular ion: $MgAr^+$. I. Observation of the $Mg(3p_\sigma)Ar^+$ B^+ state and determination of its structure and dynamics

Cite as: J. Chem. Phys. 153, 074310 (2020); doi: 10.1063/5.0015603
Submitted: 29 May 2020 • Accepted: 19 July 2020 •
Published Online: 20 August 2020

Dominik Wehrli, Matthieu Génévriez, Stefan Knecht, Markus Reiher, and Frédéric Merkt[a]

AFFILIATIONS

Laboratory of Physical Chemistry, ETH Zurich, CH-8093 Zurich, Switzerland

[a]Author to whom correspondence should be addressed: merkt@phys.chem.ethz.ch

ABSTRACT

We report on the experimental observation of the $B^+\,{}^2\Sigma^+$ state of $MgAr^+$ located below the $Mg^+(3p\,{}^2P_{3/2}) + Ar({}^1S_0)$ dissociation asymptote. Using the technique of isolated-core multiphoton Rydberg-dissociation spectroscopy, we have recorded rotationally resolved spectra of the $B^+\,{}^2\Sigma^+(v') \leftarrow X^+\,{}^2\Sigma^+(v'' = 7)$ transitions, which extend from the vibrational ground state ($v' = 0$) to the dissociation continuum above the $Mg^+(3p\,{}^2P_{3/2}) + Ar({}^1S_0)$ dissociation threshold. The analysis of the rotational structure reveals a transition from Hund's angular-momentum-coupling case (b) at low v' values to case (c) at high v' values caused by the spin–orbit interaction. Measurements of the kinetic-energy release and the angular distribution of the Mg^+ fragments detected in the experiments enabled the characterization of the dissociation mechanisms. The vibrational levels of the B^+ state above $v' = 6$ are subject to predissociation into the $Mg^+(3p\,{}^2P_{1/2}) + Ar({}^1S_0)$ continuum, and the fragment angular distributions exhibit anisotropy β parameters around 0.5, whereas direct dissociation into the continuum above the $Mg^+(3p\,{}^2P_{3/2}) + Ar({}^1S_0)$ asymptote is characterized by β parameters approaching 2. Molecular ions excited to the B^+ state with $v' = 0$–6 efficiently absorb a second photon to the repulsive part of the $^2\Sigma^+$ state associated with the $Mg^+(3d\,{}^2D_{3/2,5/2}) + Ar({}^1S_0)$ continua. The interpretation of the data is validated by the results of *ab initio* calculations of the low-lying electronic states of $MgAr^+$, which provided initial evidence for the existence of bound vibrational levels of the B^+ state and for the photodissociation mechanisms of its low vibrational levels.

I. INTRODUCTION

The ground electronic states of a large number of small molecular cations have been characterized following the development of ion-beam and ion-spectroscopy techniques.[1–10] Data concerning their electronically excited states are, however, much scarcer, in particular concerning their Rydberg states, the behavior of which is by far not as well understood as in the case of neutral molecules.

Rydberg states of neutral molecules can be described, in first approximation, as consisting of a molecular ion core in a given rovibronic state and a weakly bound Rydberg electron moving in a distant hydrogen-like $n\ell m_\ell$ orbit. The potential-energy functions of Rydberg states, thus, resemble those of the corresponding ion-core electronic state. The interaction between the Rydberg electron and the ion core rapidly decreases with an increase in n or ℓ values so that decay by predissociation and autoionization is suppressed at high n or ℓ values. The ground electronic state of most singly charged molecular cations is typically bound, either covalently or through the leading, attractive terms of the long-range electrostatic interaction series. The corresponding Rydberg states are, thus, also bound, with spectral positions following approximately Rydberg's formula,

$$\tilde{\nu} = \frac{E_I(\alpha^+)}{hc} - \frac{RZ^2}{(n-\delta_\ell)^2}. \quad (1)$$

In Eq. (1), $\tilde{\nu}$, $E_I(\alpha^+)$, R, Z, and δ_ℓ represent, respectively, the term value of the Rydberg state, the ionization energy of the molecule leading to the formation of the cation in the α^+ state, the Rydberg

constant, the charge number of the ion core (i.e., $Z = 1$ for neutral molecules), and the quantum defect of the Rydberg states with orbital angular momentum quantum number ℓ.

This overall picture of Rydberg states is also valid for molecular cations, however, with two qualitative differences, discussed here with the example of a diatomic cation AB^+, for which the ionization energy of A is higher than the ionization energy of B, as illustrated in Fig. 1. First, removal of an electron from AB^+ leads to a dication [$Z = 2$ in Eq. (1)]. Depending on whether the ionization energy of A is higher than that of B^+ or not, the ground state of the dication AB^{2+} is bound and correlates asymptotically to $A + B^{2+}$ [see Fig. 1(a)] or strongly repulsive and correlates asymptotically to $A^+ + B^+$ [see Fig. 1(b)]. Between these two limiting cases, several intermediate cases can be distinguished,[11] characterized by (avoided) curve crossings between the attractive [(i) in Fig. 1] and repulsive [(ii) in Fig. 1] potential-energy curves and by specific dynamical behaviors ranging from strongly predissociative to thermodynamically stable (see Fig. 2 of Ref. 11). Second, Rydberg states with a doubly charged ion core AB^{2+} exhibit a broader range of dynamical phenomena than those with a singly charged ion core. Whereas Rydberg series with ion-core character (i) in Fig. 1 follow Eq. (1) with $Z = 2$ and correlate diabatically to dissociation asymptotes $A + [B^{2+}]n\ell$, those with ion-core character (ii) in Fig. 1 may follow Eq. (1) with either $Z = 1$ or 2 depending on the value of n and the internuclear distance and may correlate to either $[A^+]n\ell + B^+$ or $A^+ + [B^+]n\ell$. Near-resonant charge-transfer processes are ubiquitous in this case. The Rydberg series with ion-core characters (i) and (ii) may overlap spectrally and interact, leading to situations where the decay processes can be simultaneously thought of as predissociation, autoionization, and charge transfer.

Molecular systems of the kind depicted in Fig. 1(a) are the most promising for experimental studies of Rydberg states of molecular cations. At the lowest n values, one, indeed, expects most electronic states of the singly charged cation to support metastable rovibrational levels because of the bound nature of the electronic ground state of AB^{2+} and the attractive long-range electrostatic interactions between the fragments. One can further anticipate that the alignment of the Rydberg-electron orbital with respect to the internuclear axis affects the bond strengths and the equilibrium internuclear separations of the corresponding molecular states more strongly than is the case in neutral systems. Resonant multiphoton excitation sequences through these metastable, low-n Rydberg states, thus, offer the prospect of accessing higher-lying Rydberg series of the cations over a broad range of internuclear separations and energies, all the way to the second ionization thresholds.

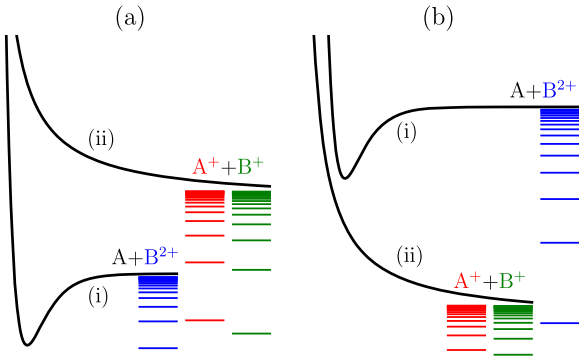

FIG. 1. Schematic representation of the electronic states of AB^{2+} dissociating in $A + B^{2+}$ and $A^+ + B^+$ fragments for the cases where the ionization energy of B^+ is lower than that of A [panel (a)] and vice versa [panel (b)]. The horizontal bars indicate atomic Rydberg series converging to the atomic ions A^+ (red), B^+ (green), and B^{2+} (blue).

$MgAr^+$ is an ideal system for a global investigation of the Rydberg states of a molecular cation. The lowest molecular states of $MgAr^+$ derived from Mg^+ 3s, 3p, and 3d configurations possess Rydberg character in the sense of Mulliken,[12] and their overall energy-level structure follows that of Mg^+. The ionization energy of Ar [127 109.842(4) cm^{-1}[13]] lies higher than that of Mg^+ [121 267.65(6) cm^{-1}[14]], corresponding to the situation depicted in Fig. 1(a). $MgAr^+$ has only 29 electrons, and accurate *ab initio* calculations can be carried out, also for electronically excited states, to guide the experimental investigations. Potential energy functions have been reported for several of the low-lying electronic states of $MgAr^+$.[15–22] These states can be labeled by the state of the Mg^+ or Ar^+ ion at the dissociation asymptote in addition to the usual letters and term symbols used to designate electronic states of diatomic molecules. In this nomenclature, the first electronic states of $MgAr^+$ are the $Mg(3s)Ar^+$ $X^+\,^2\Sigma^+$, $Mg(3p_\pi)Ar^+$ $A^+\,^2\Pi_{1/2}$ and $^2\Pi_{3/2}$, and $Mg(3p_\sigma)Ar^+$ $B^+\,^2\Sigma^+$ states, which are referred to below as X^+, $A^+_{1/2}$, $A^+_{3/2}$, and B^+ states. These labels are independent of the angular-momentum coupling cases, which depend on the internuclear separation, as discussed in Sec. IV A. The $A^+_{1/2}$, $A^+_{3/2}$, and B^+ states form the 3p Rydberg complex discussed in this article. The Rydberg states of $MgAr^+$ associated with the Mg^+ 3p, 3d, and 4s dissociation asymptotes are easily accessible from the X^+ ground state through single-photon or resonant two-photon excitation processes involving commercial UV lasers (see Fig. 2). The first electronically excited state, the A^+_Ω ($\Omega = 1/2, 3/2$) state, has a binding energy of more than 0.5 eV and an equilibrium internuclear distance of 2.40 Å. It is metastable, and several of its vibrational levels have been observed by high-resolution spectroscopy.[23–27] The other member of the 3p Rydberg complex, the B^+ state, is expected from calculations to be only very weakly bound and to have a much larger equilibrium separation (~4.37 Å, see Sec. III). In the case of a sufficiently long lifetime of the B^+ state, the members of the 3p complex would provide a set of intermediate states ideally suited to access higher Rydberg states of $MgAr^+$ over a broad range of internuclear distances. The complete characterization of this complex, which is the subject of this article and Paper II,[28] represents the first step in our efforts toward obtaining a global picture of the Rydberg series of a molecular cation.

The present article reports on the experimental observation of the B^+ state of $MgAr^+$ and on the characterization of its structure and predissociation dynamics. The experimental setup and methods used to record spectra of the B^+ state and to study its predissociation are described in Sec. II. Section III presents the computational methods that have been used to calculate the potential-energy functions of the low-lying electronic states of $MgAr^+$ *ab initio*. The experimental data obtained on the B^+–X^+ band system, which include high-resolution spectra for the determination of rovibrational level energies and fragment time-of-flight (TOF) spectra for the

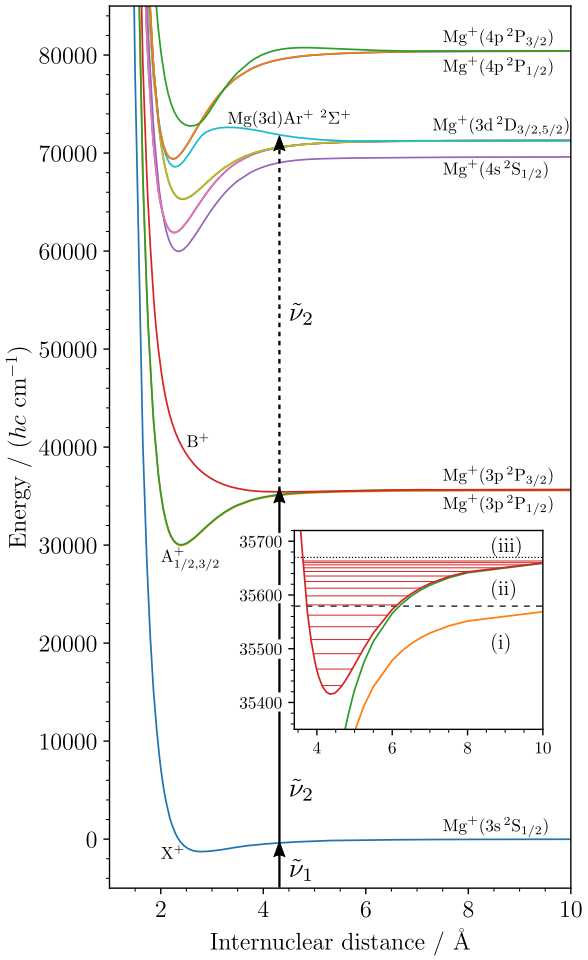

FIG. 2. Potential-energy curves of the ground and lowest-lying excited states of $MgAr^+$ obtained from relativistic EOM-CCSD/X2Cmmf/5Z* calculations. The inset presents an enlargement of the B^+ state curve. The configuration and term symbol of the resulting Mg^+ ion in the asymptotic limit are indicated for each group of molecular electronic states. Ar is in its $^1S_0$ ground state in each case. The solid arrows indicate the laser excitation scheme used in the experiment, and the dashed arrow presents a possible pathway of resonant multiphoton dissociation. The spectral regions designated (i), (ii), and (iii) in the inset are introduced in Sec. IV B.

determination of dissociation energies and β parameters, are presented, analyzed, and discussed in Sec. IV. These data, together with similar data obtained on the A^+–X^+ band system of $MgAr^+$, form the basis of the global analysis of the 3p Rydberg complex of $MgAr^+$ summarized in Paper II.[28] Together, these two articles complete our first step toward the characterization of the Rydberg spectrum of a molecular cation.

II. EXPERIMENT

The experimental setup has been described in detail in Refs. 14 and 29. It consists of a laser-ablation source of Mg atoms, two Nd:YAG-pumped pulsed dye lasers (pulse duration ~5 ns), and a detection system for the photoions produced following photoexcitation. In the source, the ablated atoms were entrained in a supersonic beam of Ar, in which MgAr molecules were formed in the Mg(3s3p)Ar a $^3\Pi_0$ state and rotationally cooled to below 5 K. The formation of MgAr in the metastable Mg(3s3p)Ar a $^3\Pi_0$ state was first described by Bennet *et al.*,[30] who used a similar laser-ablation source and also observed the MgAr singlet ground state.[31] The molecular beam passed through a 3-mm-diameter skimmer and entered the photoexcitation chamber, where it was intersected by two laser beams at right angles. Photoexcitation took place within an electrode stack that allowed the application of pulsed electric fields to field ionize high Rydberg states and extract photoions into a time-of-flight (TOF) mass spectrometer at the end of which they were detected using a micro-channel-plate (MCP) assembly.

The output of the first laser was frequency-tripled using two BBO crystals and set to a wave number $\tilde{\nu}_1 = 39\,334.8$ cm^{-1}. The frequency-tripled radiation had a bandwidth of ~0.15 cm^{-1}, and the laser pulse energy was ~0.5 mJ. The wave number $\tilde{\nu}_2$ of the second laser, after frequency doubling with a BBO crystal, was tunable in the range from 36 100 cm^{-1} to 36 700 cm^{-1}. The frequency-doubled radiation had a bandwidth of ~0.1 cm^{-1}, the beam diameter was ~1 mm, and the pulse energy could be adjusted from below 1 μJ up to ~0.5 mJ. The wave numbers of the lasers were calibrated using a commercial wavemeter with a specified absolute accuracy of 0.02 cm^{-1}.

The first laser was used to excite MgAr to $[X^+(v'' = 7)]n\ell$ Rydberg states with principal quantum numbers around $n \sim 135$. After ~10 ns, the ionic core of the MgAr Rydberg molecules was excited from the $X^+(v'' = 7)$ to the B^+ state using the second laser (see the solid arrow in Fig. 2). Dissociation of the ion core in the B^+ state, either by direct or indirect mechanisms as discussed below, led to the formation of Mg atoms in high Rydberg states.[27] Photoions generated in the photoexcitation region by the laser pulses (prompt ions) could be separated from the Mg Rydberg atoms by applying a ~5-μs-long electric-field pulse of −1.7 V/cm, the magnitude of which is not large enough to efficiently field ionize Rydberg states with $n \sim 135$. A subsequent electric-field pulse with field strengths in the range from 50 V/cm to 170 V/cm field ionized the Rydberg states for detection. The spatial separation of the high Rydberg states and the prompt ions enabled us to distinguish the two sets of ions by their times of flight. Recording the pulsed-field-ionization yield of Mg^+ as a function of the laser wave number allowed the background-free measurement of transitions from a state-selected vibrational level of the X^+ electronic ground state of $MgAr^+$ to electronically excited levels,[27] in the present case the $MgAr^+$ B^+ state.

Using extraction field pulses of 50 V/cm, we observed a structure in the TOF spectrum of field-ionized Mg^+ ions reflecting the velocity and the angular distribution of the dissociation products. The situation is depicted schematically in Fig. 3, which presents the photoexcitation region and the TOF mass spectrometer. Neutral Mg Rydberg fragments flying toward or away from the detector had different times of flight because of (i) the different distances to the detector after dissociation resulting from the ~5-μs-long cloud expansion following photoexcitation and (ii) the different extraction potentials they were subjected to, resulting from the different positions in the electrode stack. In the case where the dissociation fragments were preferentially released along the extraction axis, two distinct peaks were observed in the TOF spectrum, an example of

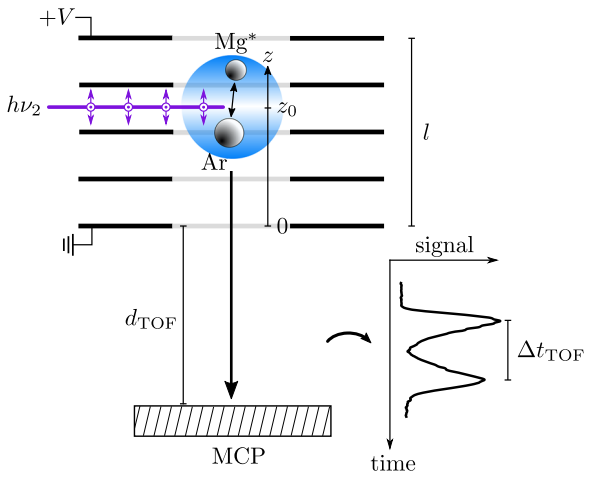

FIG. 3. Schematic representation of the photoexcitation region and the TOF mass spectrometer. After excitation with the second laser (indicated by ν_2), the MgAr molecules dissociate at position z_0, and the Mg-Rydberg-fragment cloud expands until the atoms are ionized by a pulsed electric field, which accelerates the Mg^+ ions to the MCP. The angular distribution of the dissociation products leads to TOF spectra such as the one shown at the bottom right (see text for details).

which is shown at the bottom right of Fig. 3. Conversely, in the case where the dissociation fragments were preferentially released perpendicular to the extraction axis, only one broad peak was observed in the TOF spectrum.

We developed a model that allowed us to determine from the TOF spectra the angular distribution of the dissociation fragments and the kinetic-energy release (KER) resulting from the dissociation. The velocity of the Mg^+ fragments after the dissociation is related to the KER by

$$v = \sqrt{\frac{2 \cdot \mathrm{KER} \cdot m_{\mathrm{Ar}}}{m_{\mathrm{Mg}}(m_{\mathrm{Mg}} + m_{\mathrm{Ar}})}}, \tag{2}$$

where m_{Mg} and m_{Ar} are the masses of Mg and Ar, respectively. We designate the position of the dissociation event in the electrode stack as z_0 (see Fig. 3) and the difference between the time at which dissociation occurs and the time at which the large electric field pulse is applied to field ionize the Rydberg atoms and accelerate the ions toward the detector as Δt_{prep}. The vertical position z of the Mg^+ fragments in the stack at the time of extraction is given by

$$z = z_0 + \Delta t_{\mathrm{prep}}(v \cos\theta_z - v_{\mathrm{beam}}), \tag{3}$$

where θ_z is the angle between the z axis and the direction of dissociation and v_{beam} is the velocity of the molecular beam. The time of flight t_{TOF} resulting from an extraction field with magnitude $F(=V/l)$ is in good approximation, given by

$$t_{\mathrm{TOF}}(z) = t_0 + \frac{d_{\mathrm{TOF}} + 2z}{\sqrt{2qFz/m_{\mathrm{Mg}}}}, \tag{4}$$

where t_0 is the extraction time, d_{TOF} is the distance between the electrode stack and the MCP, and $q = +e$ is the charge of Mg^+. The angular distribution of the fragments after one-photon direct dissociation is given by[32]

$$\mathrm{d}I(\Omega) = \frac{I_0}{4\pi}[1 + \beta P_2(\cos\theta)]\mathrm{d}\Omega, \tag{5}$$

where I_0 is the total intensity, β is the anisotropy parameter, θ denotes the angle between the direction of dissociation and the direction of polarization of the laser beam, P_2 is the Legendre polynomial of second order, and $\mathrm{d}\Omega$ denotes the solid-angle differential element. In our experiments, the laser polarization was either parallel or perpendicular to the z axis. Using Eqs. (3) and (4) and integrating over the azimuthal angle around the z axis, we can express $\mathrm{d}I$ as a function of t_{TOF}, which, for a laser polarization parallel to the z axis, gives

$$\mathrm{d}I(t_{\mathrm{TOF}}) = \frac{I_0}{2\Delta t_{\mathrm{prep}} v}\left[1 + \beta P_2\left(\frac{z(t_{\mathrm{TOF}}) - z_0'}{\Delta t_{\mathrm{prep}} v}\right)\right] \times \left|\frac{\mathrm{d}z}{\mathrm{d}t_{\mathrm{TOF}}}\right| \mathrm{d}t_{\mathrm{TOF}}. \tag{6}$$

In Eq. (6), $z_0' = z_0 - \Delta t_{\mathrm{prep}} v_{\mathrm{beam}}$. The expression for $\mathrm{d}I(t_{\mathrm{TOF}})$ when the laser polarization is perpendicular to the z axis is obtained by replacing β by $-\beta/2$ in Eq. (6) (see Appendix A). The finite intersection volume of the molecular and the laser beams has a significant effect on the TOF spectra and was taken into account following the procedure presented in Appendix A, which consisted in summing the TOF profiles originating from different parts of the photoexcitation volume. After a baseline correction with a second-order polynomial, we could determine β and the KER in a nonlinear least-squares fit of the experimental TOF spectra. The extraction time t_0 and the effective distance d_{TOF} [see Eq. (4)] of the electrode stack to the MCP were calibrated by matching simulated TOF spectra to experimental TOF spectra recorded at known KERs.

The model described above relies on the use of Eq. (5), which is not valid for multiphoton dissociation.[33] Therefore, we also used an alternative method for determining the KER, which is independent of the exact form of the angular distribution. The KER is related to the photon wave number $\tilde{\nu}_2$ and the dissociation limit E_{D} (given in the wave number unit cm^{-1}) by $\mathrm{KER}/(hc) = \tilde{\nu}_2 - E_{\mathrm{D}}$. We consider the case where the laser polarization is parallel to the z axis. By defining $\Delta t_{\mathrm{TOF}} = t_{\mathrm{TOF}}(z(\theta)) - t_{\mathrm{TOF}}(z(-\theta))$, where $t_{\mathrm{TOF}}(z)$ is defined as in Eq. (4), we find for Δt_{TOF} a function of the form

$$\Delta t_{\mathrm{TOF}}^2(\tilde{\nu}_2) = a^2(\tilde{\nu}_2 - E_{\mathrm{D}}) + b^2(\tilde{\nu}_2 - E_{\mathrm{D}})^3 + 2ab(\tilde{\nu}_2 - E_{\mathrm{D}})^2 \tag{7}$$

in the limit of low KER. The TOF differences Δt_{TOF} can be determined from experimental TOF spectra, as shown in Fig. 3. The quantities a, b, and E_{D} were determined in a nonlinear least-squares fit of Eq. (7) to Δt_{TOF} values measured at different wave numbers $\tilde{\nu}_2$.

III. QUANTUM-CHEMICAL CALCULATIONS

A. Computational methodology

To characterize the ground and low-lying excited states of the $MgAr^+$ ion, we carried out relativistic *ab initio* calculations with *variationally* treated spin–orbit coupling (SOC) at various Mg–Ar internuclear distances. As wave-function models we chose relativistic equation-of-motion coupled-cluster with singles and doubles excitations (EOM-CCSD),[34] Kramers-restricted multi-reference configuration interaction with singles and doubles excitations (KR-MRCI-SD),[35,36] and relativistic matrix product states (MPS) optimized with

the density-matrix-renormalization-group (DMRG) algorithm.[37,38] All three models have different advantages and disadvantages. Whereas the EOM-CCSD calculations are considered to be very accurate in combination with a large single-particle basis set, the multi-reference and DMRG calculations probe the validity of the EOM-CCSD wave-function model, but require us to resort to smaller basis sets so that only semi-quantitative accuracy can be achieved in the latter calculations.

All DMRG and KR-MRCI-SD calculations were carried out within a four-component Dirac Hamiltonian framework including two-electron Coulomb contributions [denoted as Dirac–Coulomb (DC) in the following] and with uncontracted aug-cc-pVDZ basis sets[39] (denoted as DZ*) for Mg and Ar, respectively. Furthermore, they share a common reference wave function, which was obtained from an average-of-configuration self-consistent-field calculation[40] for the open-shell $MgAr^+$ ion, namely, by taking into account all possible configurations of one electron in 26 Kramers-paired spinors. In the ensuing correlation step, all electrons originating from the outer-valence Ar 3p and Mg 3s shell were correlated in an orbital space spanned by 47 Kramers pairs (corresponding to 94 molecular spinors). In contrast to the DMRG approach, the correlation space for the KR-MRCI-SD approach was further divided into two orbital spaces. For KR-MRCI, the reference space comprised all spinors of the Ar 3p shell as well as the corresponding 26 spinors of the average-of-configuration space of the preceding self-consistent-field step. The second orbital space then contained all remaining, energetically lowest-lying 62 spinors while taking into account at most singles and doubles excitations between the two orbital spaces. The DMRG calculations delivered a full configuration interaction model in the given orbital space and served as a qualitative reference for the KR-MRCI-SD model near the dissociation limit at an internuclear distance of $R = 50$ Å. In the relativistic DMRG calculations, the maximum virtual bond dimension m was set to $m = 1024$ in combination with orbitals ordered according to their energy, a maximum of 15 back-and-forward sweeps as well as a random guess for the initial MPS.

For the EOM-CCSD model, a closed-shell reference wave function was obtained for each of the three distinct cases described below from self-consistent-field calculations for a doubly ionized $MgAr^{2+}$ molecular ion. This allowed us to calculate the electronic ground and electronically excited states of $MgAr^+$ as the electron-attached states to $MgAr^{2+}$. We then performed three types of EOM-CCSD calculations: the first one, EOM-CCSD/DC/2Z*, comprised the same Hamiltonian, DZ*-type one-particle basis sets, and a correlation space of seven electrons in 94 spinors as described above for the KR-MRCI-SD and DMRG models. In contrast, our second set takes into account the full correlation space, i.e., correlating all 29 electrons of the $MgAr^+$ molecular ion in the complete set of molecular spinors spanned by the atom-centered, uncontracted DZ*-type basis sets for Mg and Ar. Finally, our third type of EOM-CCSD calculations, denoted as EOM-CCSD/X2Cmmf/5Z*, was based on a molecular-mean-field (mmf) exact-two-component (X2C) Hamiltonian[41] including two-electron Coulomb and Gaunt contributions in combination with very large, fully uncontracted aug-cc-pV5Z basis sets[39] (denoted as 5Z*) for Mg and Ar [similar to the second set, all electrons of Mg (ion) and Ar (atom) were correlated within the set of molecular spinors up to an energy threshold of 100 Hartree that result from the 5Z* basis sets for Mg and Ar in their uncontracted form].

All EOM-CCSD and the KR-MRCI-SD calculations were carried out with a development version of the DIRAC19 program package.[42,43] This program also provides an interface that steers relativistic DMRG calculations with the DMRG software package QCMAQUIS.[38,44,45] Molecular constants have been derived by a least-squares fit of the potential energy curves to a fifth-order polynomial by means of the TWOFIT utility program available in DIRAC19.

B. Numerical results

Table I presents the atomic low-lying excited-state spectrum of Mg^+ at the dissociation limit of $MgAr^+$, as obtained from

TABLE I. Energy levels of the Mg^+ ion obtained from molecular four-component KR-MRCI-SD/DC/DZ*, DMRG/DC/DZ*, and EOM-CCSD/DC/DZ* as well as molecular-mean-field two-component EOM-CCSD/X2Cmmf/5Z* calculations for $MgAr^+$ at an internuclear distance of $R = 50$ Å. All term values are reported relative to the ground state in cm^{-1}.

			Method[a]					
Conf.	Term	J	KR-MRCI-SD/DZ*	DMRG/DZ*	EOM-CCSD/DZ*	EOM-CCSD/DZ*[c]	EOM-CCSD/5Z*	Reference[b]
3s	^2S	1/2	0.0	0.0	0.0	0.0	0.0	0.0
3p	^2P	1/2	34 703	34 703	34 680	35 013	35 579	35 669
		3/2	34 793	34 793	34 769	35 104	35 670	35 761
4s	^2S	1/2	68 131	68 131	68 097	68 494	69 618	69 805
3d	^2D	5/2	70 861	70 861	70 818	71 300	71 294	71 490
		3/2	70 861	70 861	70 819	71 300	71 295	71 491
4p	^2P	1/2	80 308	80 308	80 270	80 735	80 411	80 620
		3/2	80 344	80 344	80 306	80 772	80 442	80 650

[a]The notation indicating the dependence on the Hamiltonian has been dropped in the labeling of the methods.
[b]Data taken from the NIST Basic Atomic Spectra Database; see Ref. 46.
[c]EOM-CCSD/DC/DZ* calculations with full correlation space.

molecular KR-MRCI-SD/DC/DZ*, DMRG/DC/DZ*, and EOM-CCSD/DC/DZ* and EOM-CCSD/X2Cmmf/5Z* calculations carried out at an internuclear distance of R = 50 Å. The calculated excited-state data for Mg^+ are, in general, in reasonably good agreement with the corresponding reference data taken from the standard NIST atomic spectra database.[46] As expected, we find a clear improvement of the calculated results when switching from the small DZ* basis sets to the basis set limit achieved by the uncontracted 5Z* basis set.

As can be seen from Table I, the largest absolute deviation of ~1700 cm^{-1} (corresponding to a relative error of 2.5%) with respect to the reference data is found for the 4s excited state of Mg^+ in the case of the EOM-CCSD/DC/DZ* model and, similarly, for the KR-MRCI-SD/DC/DZ* and DMRG/DC/DZ* approaches. The DMRG data exactly match with KR-MRCI-SD for the Mg excited states because these states are effectively one-electron states at the dissociation limit with little to no Ar 3p correlation contributions. In other words, both approaches yield results of near full-configuration-interaction quality for the Mg-dominated states at the dissociation limit because of the chosen correlation space. The situation changes for the charge-transfer states, which will be discussed in future work.

The deviation of 2.5% reduces to less than 0.3% for our EOM-CCSD/X2Cmmf/5Z* reference model. A further comparison with the EOM-CCSD/DC/DZ* model illustrates that this considerable improvement within our reference model is a combined result of both the enlarged one-particle basis sets and the inclusion of core–valence and core–core electron correlation. For example, solely taking into account the latter correlation effects within the EOM-CCSD/DC/DZ* approach (seventh column in Table I) reduces the relative error to only 1.9% for the previously discussed 4s excited state of Mg^+. Moreover, resorting to fully uncontracted aug-cc-pCV5Z basis sets[47,48] (c5Z*, not shown in Table I), which include in addition to the 5Z* sets of primitive functions optimized tight core-polarizing basis functions, further reduces the deviation for the 4*s* excited state of Mg^+ from 0.3% (EOM-CCSD/X2Cmmf/5Z*) to 0.1% (EOM-CCSD/X2Cmmf/c5Z*). In general, we find that the inclusion of tight core-polarizing basis functions improves the description of the Mg-dominated excited states, i.e., leading to an even closer agreement with the reference data, with excitation-energy shifts ranging from 35 cm^{-1} (the $3s^0 3p\,^{12}P$ term) to 158 cm^{-1} (the $3s^0 3d\,^{12}D$ term).

Particularly noteworthy is that all computational approaches considered in this work yield spin–orbit splittings of both low-lying ^2P atomic terms, corresponding to a $3s^0 3p^1$ and $3s^0 4p^1$ configuration of the Mg^+ ion, respectively, that are in excellent agreement with their respective experimental reference values, as shown in Table I.

Figure 2 shows the low-lying potential energy curves of the ground and lowest-lying excited states of $MgAr^+$ obtained with the EOM-CCSD/X2Cmmf/5Z* approach. Note that we here only consider those electronic states of the $MgAr^+$ ion which correspond, in the asymptotic limit, to an argon atom in its ground state and a Mg^+ ion in its ground and excited state up to the Mg^+ $3s^0 4p^1$ configuration. Electronic states with a predominant Ar → Mg^+ charge-transfer character, which correspond, in the asymptotic limit, to an Ar^+ ion (the $3s^2 p^5\,^2P$ term) and a $Mg(3s^2)$ ground-state atom, will be discussed in future work.

As can be understood in view of Fig. 2, the lowest-lying electronically excited $^2\Pi$ and $^2\Sigma^+$ states arise from excitations to a Mg^+ 3p orbital, which can exhibit perpendicular (p_π) and parallel (p_σ) orientations with respect to the molecular axis. Hence, electrostatic interactions in the excited $A^+_{1/2,3/2}$ states are expected to be relatively strong because of the orientation of the involved Mg p_π orbital, which effectively exposes a doubly positive Mg core to the Ar atom.[49] In contrast, as a result of on-axis electron-density contribution originating from the occupation of on-axis σ-type orbitals, electrostatic binding is reduced in the Mg 3s-like X^+ ground and excited $3p_\sigma$-like B^+ states. In the latter, a greater shielding is to be expected relative to the ground state.[24] Consequently, we expect the $A^+_{1/2,3/2}$ states to be more strongly bound than the X^+ ground state, giving rise to a redshift of the $A^+_{1/2,3/2} \leftarrow X^+$ electronic transitions with respect to the atomic resonance line. Likewise, as a result of weaker electrostatic interactions, the excited B^+ state is more weakly bound than the ground state. The latter implies a blue-shifted $B^+ \leftarrow X^+$ transition relative to the atomic resonance.[24] Similar qualitative considerations hold for the higher-lying $^2\Sigma$, $^2\Pi_{1/2,3/2}$, and $^2\Delta_{3/2,5/2}$ states of $MgAr^+$ that correlate, in the asymptotic limit, with an Ar ground-state atom and a $Mg^+(4s)$, $Mg^+(3d)$, and $Mg^+(4p)$ excited-state ion, respectively.

In agreement with the above qualitative considerations, inspection of Fig. 2 reveals that the spin–orbit split Ω = 1/2 and Ω = 3/2 components of the $A^+_{1/2,3/2}$ state are more strongly bound than the X^+ ground state. In addition, we find that their excited-state equilibrium internuclear distance of $R_e(A^+)$ = 2.396 Å is considerably shorter than the predicted ground-state equilibrium internuclear distance of $R_e(X^+)$ = 2.803 Å. Both of these results are, therefore, consistent with the qualitatively expected redshift of the $A^+_{1/2,3/2} \leftarrow X^+$ electronic transitions discussed above. Based on these findings, our EOM-CCSD/X2Cmmf/5Z* data yield an estimate for the $A^+ \leftarrow X^+$ transition of 31 402 cm^{-1}. This value agrees very well with the corresponding data for the spin–orbit averaged $\tilde{\nu}_{00}$ transition of 31 477 cm^{-1} obtained from resonance-enhanced multiphoton dissociation measurements.[27] Considering the calculated $\tilde{\nu}_{00}$ transition as a reference, we, therefore, predict a redshift in the $MgAr^+$ spectrum for the corresponding Mg^+ $3p\,^2P_{1/2,3/2} \leftarrow 3s\,^2S_{1/2}$ transition in the bare ion to be approximately 4300 cm^{-1}. Our calculated result matches closely the experimental data mentioned above, which yield a redshift of 4253 cm^{-1}. Moreover, our estimate for the dissociation energy D_0 = 1220.2 cm^{-1} of the X^+ ground state is in very good agreement with the experimental value of D_0 = 1246.0(12) cm^{-1} reported in Paper II.[28]

Turning to the excited-state manifold corresponding, in the asymptotic limit, to a Mg^+ $3s^0 3d^1$ configuration, as shown in Fig. 2, we find that the spin–orbit splitting of the $^2\Pi$ and $^2\Delta$ states is too small to resolve the spin–orbit-split components in Fig. 2. In agreement with the qualitative considerations given above, the $^2\Pi_{1/2,3/2}$ and $^2\Delta_{3/2,5/2}$ states (displayed with yellow and pink lines in Fig. 2, respectively) are more strongly bound than the X^+ state because of the off-axis electron density that results from the occupation of $3d_\pi$- or $3d_\delta$-like orbitals of the Mg^+ ion. Interestingly, the $^2\Sigma$ state originating from a Mg^+ $3s^0 3d^1$ configuration (the cyan line) undergoes an avoided crossing at an internuclear distance of ~2.8 Å, with a higher-lying $^2\Sigma$ state (the upper green line) that correlates, in the asymptotic limit, to a Mg^+ $3s^0 4p^1$ configuration.

IV. EXPERIMENTAL RESULTS AND DISCUSSION

A. Energy-level structure

We have measured the photodissociation spectrum of the $MgAr^+$ $X^+(v'' = 7)$ state via the $B^+(v')$ state using the method of isolated-core (multi)photon Rydberg-dissociation spectroscopy.[27] Our measurements include overview spectra of the complete vibrational progression of the B^+ state as well as high-resolution measurements of each vibrational band, in which the rotational structure could be partially resolved. The assignment of the vibrational quantum number was derived from the comparison with the corresponding spectrum of $^{26}MgAr^+$ (not shown), as explained below.

Figure 4 depicts an overview spectrum of the $^{24}MgAr^+$ $B^+(v') \leftarrow X^+(v'' = 7)$ transitions recorded at high laser-pulse energies (~0.5 mJ per pulse). The vibrational progression exhibits a drop in intensity around $v' = 6$ and extends all the way to the dissociation continuum, the onset of which is indicated by a rise in the signal around 36 409 cm^{-1}. The intensity maxima of the strongest vibrational bands, in particular, $v' = 1$, 3, and $v' \geq 9$, are approximately the same, which suggests that the spectrum was recorded under saturating conditions, which were necessary to observe all vibrational levels of the B^+ state, especially those of low v' values. Although the overview spectrum in Fig. 4 only allows the unambiguous assignment of B^+ levels up to $v' = 17$, several levels beyond $v' = 17$ could be identified with the help of spectra recorded at lower pulse energies and higher resolution (see below). The analysis of the vibrational intensity distribution is presented in Sec. IV D.

To assign the vibrational quantum numbers, we determined the positions $\tilde{\nu}^i(v')$ ($i = 24$, 26) of the band maxima for both $^{24}MgAr^+$ and $^{26}MgAr^+$ and extracted the isotopic shifts of the $B^+(v')$ levels using

$$\Delta\tilde{\nu}(v') = \Delta_a + (\tilde{\nu}^{24}_{X^+}(7) - \tilde{\nu}^{26}_{X^+}(7)) + (\tilde{\nu}^{24}(v') - \tilde{\nu}^{26}(v')). \quad (8)$$

In Eq. (8), $\Delta_a = 0.38$ cm^{-1} is the isotopic shift of the MgAr a $^3\Pi_0(v = 0)$ state, estimated from the results of *ab initio* calculations reported in Ref. 21, and $\tilde{\nu}^i_{X^+}(v'' = 7)$ denote the $^iMgAr^+$ $X^+(v'' = 7) \leftarrow {}^iMgAr$ a $^3\Pi_0(v = 0)$ transition wave numbers.[29,49] For instance, the isotopic shift we observed for $v' = 7$ is $\Delta\tilde{\nu}(7) = 3.3(3)$ cm^{-1}. This standard analysis of isotopic shifts[50] did not only yield an unambiguous vibrational assignment but also values for the harmonic [$\omega_e = 35.43(30)$ cm^{-1}] and anharmonic [$\omega_e x_e = 1.21(20)$ cm^{-1}] vibrational constants of the $^{24}MgAr^+$ B^+ state, which adequately describe the observed structure up to $v' = 12$.

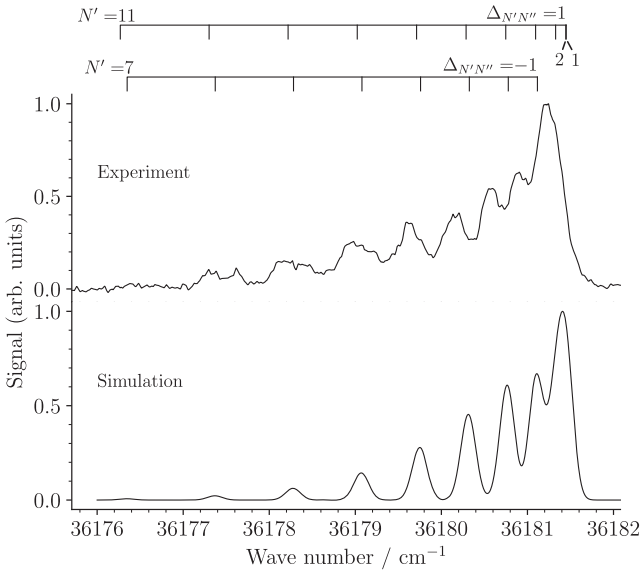

FIG. 5. High-resolution spectrum of the $MgAr^+$ $B^+(v' = 1) \leftarrow X^+(v'' = 7)$ band. The initial and the final states are well described by Hund's case (b), leading to two branches that overlap in the spectrum. The branches are denoted by $\Delta_{N'N''} = N' - N'' = 1$ (R-branch) and $\Delta_{N'N''} = -1$ (P-branch), where N'' and N' are the rotational-angular-momentum quantum numbers of the initial and final states, respectively. The simulation was performed assuming a rotational temperature of 2 K.

The upper panel of Fig. 5 shows a spectrum of the $B^+(1) \leftarrow X^+(7)$ band recorded at high resolution. The spectrum exhibits a strong line on the high-wave-number side and a progression of transitions to different rotational states of the B^+ state with intensities decreasing toward the low-wave-number end of the spectrum. This spectrum is typical of what we observed for transitions to the lowest vibrational levels of the B^+ state. Beyond $v' = 7$, the spectra revealed a different rotational structure, examples of which are shown in the upper panel of Fig. 6 for $v' \geq 13$. In this region, the vibrational bands comprise more lines. We attribute this change to the increasing importance of the spin–orbit interaction as the

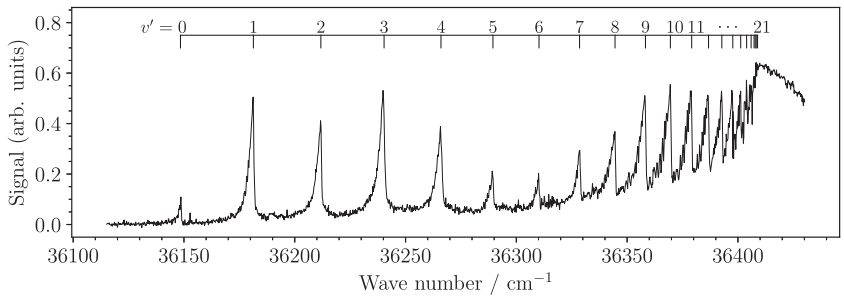

FIG. 4. Overview spectrum of the $^{24}MgAr^+$ $B^+(v') \leftarrow X^+(v'' = 7)$ transition recorded at high laser-pulse energies (~0.5 mJ per pulse). The sharp rise around 36 409 cm^{-1} indicates the onset of the dissociation continuum of the B^+ state. In this spectrum, only vibrational levels up to $v' = 17$ are resolved. The positions of the remaining vibrational levels, indicated along the assignment bar, were derived from the high-resolution spectrum shown in Fig. 6.

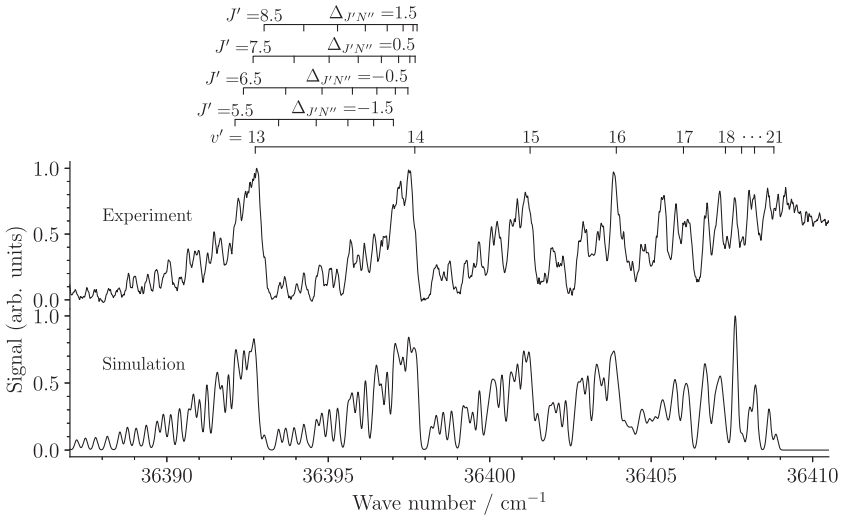

FIG. 6. High-resolution spectrum of the $MgAr^+$ $B^+(v' = 13–21) \leftarrow X^+(v'' = 7)$ bands. In this range, the final states are well described by Hund's case (c), leading to four rotational branches. The branches are denoted by half-integer values of $\Delta_{J'N''} = J' - N''$, where N'' is the rotational-angular-momentum quantum number of the initial state and J' is the total angular momentum of the final states. The simulation was performed assuming a rotational temperature of 3 K.

internuclear separation R increases and the resulting mixing of the B^+ and $A^+_{1/2}$ states at large R values. This mixing leads to a transition from Hund's case (b) at short internuclear distances and low values of v', characterized by integer values of the rotational-angular-momentum quantum number N', to Hund's case (c) at large internuclear distances and high values of v', characterized by half-integer values of the total angular momentum quantum number J'. A complete model of the spin–orbit interaction in the $Mg(3p)Ar^+$ Rydberg complex is presented in Paper II.[28]

For each of the $v' = 0–3$ and $v' = 7–16$ bands, we were able to identify several isolated rotational lines and determined their positions $\tilde{\nu}$ by fitting them with Gaussian line-shape functions. We then determined rotational constants and the band origin $\tilde{\nu}_{v'7}$ by performing nonlinear least-squares fits of the appropriate expression for the transition energy. Because of the progressive evolution of the rotational structure from Hund's case (b) at low v' values to Hund's case (c) at high v' values, the choice of the appropriate Hund's case for intermediate v', namely, $v' = 8–12$, was not completely unambiguous. Up to $v' = 8$, we used the following expression:

$$\tilde{\nu} = \tilde{\nu}_{v'7} + B'_{v'}N'(N'+1) - B''_7N''(N''+1), \tag{9}$$

describing a Hund's-case-(b)-to-Hund's-case-(b) transition at the low N' and N'' values probed experimentally. In Eq. (9), $B'_{v'}$, N' and B''_7 (=0.1121 cm^{-1}[28]), N'' are the rotational constants and rotational quantum numbers of the final and initial states, respectively. The band origins and rotational constants determined in this way are listed in Table II and were used to calculate the spectra for comparison with experimental results. An example is shown for v' = 1 in Fig. 5 for a rotational temperature of 2 K. The spectrum consists of two overlapping branches, denoted by $\Delta_{N'N''} = N' - N''$ above the assignment bars. The $\Delta_{N'N''} = 0$ branch is missing, as expected for a Σ^+–Σ^+ transition. The degradation of the band intensity profile toward low wave numbers results from the different rotational constants of the initial (B''_7 = 0.1121 cm^{-1}) and final states (B'_1 = 0.0550 cm^{-1}). Whereas the calculated spectrum in Fig. 5 assumes a thermal distribution, the experimental spectrum was recorded from the nonthermal distribution generated with the laser driving the $X^+(7) \leftarrow$ a $^3\Pi_0$ transition. Therefore, the intensity distribution of the calculated spectrum does not reliably describe the measured intensity distribution, and the effect is particularly pronounced near the R-branch bandhead.

Beyond $v' = 8$, we used the standard expression for transitions between a Hund's case (b) initial level and a Hund's case (c) final level,

$$\tilde{\nu} = \tilde{\nu}_{v'7} + B'_{v'}\left[J'(J'+1) - \Omega'^2\right] - B''_7N''(N''+1), \tag{10}$$

where J' is the total angular momentum of the final state and $\Omega' = 1/2$. The band origins and rotational constants determined in least-squares fits based on Eq. (10) are given in Table II. Calculations of the rotational structure of Hund's-case-(b)-to-Hund's-case-(c) transitions for $v' \geq 13$ at a rotational temperature of 3 K are shown in the lower panel of Fig. 6, with explicit rotational assignments for the $v' = 14$ band. Each band consists of four branches, denoted as $\Delta_{J'N''} = J' - N''$, instead of two at low v', which explains the different appearance of the bands observed at low and high v' values.

For the $v' = 4–6$ vibrational states, we could not resolve individual rotational lines. To determine the band origins listed in Table II, we simulated the band contours assuming a Hund's-case-(b)-to-Hund's-case-(b) transition and rotational constants obtained by polynomial interpolation of the rotational constants listed in Table II and shifted the calculated spectra along the wave-number axis until agreement with the experimental observations was reached. From the $B'_{v'}$ values determined for the $v' = 0–8$ vibrational levels, a B_e value of 0.0608(7) cm^{-1} was derived. This corresponds to an equilibrium bond length R_e of 4.301(25) Å, which is in reasonable agreement with the theoretical value of 4.374 Å. From the origin of the $B^+(0) \leftarrow X^+(7)$ band [$\tilde{\nu}_{07}$ = 36 148.43(20)] and the onset of the dissociation continuum in Fig. 6, i.e., E_D = 36 409.0(10) cm^{-1}, we estimate the dissociation energy of the B^+ state to be D_0 = 260.6(10) cm^{-1}. Using the vibrational constants listed above, we derive an equilibrium dissociation energy of $D_e = D_0 + \omega_e/2 - \omega_e x_e/4$ = 278.0(10) cm^{-1} for the B^+ state. These values of D_0 and D_e are in reasonable agreement with the values of 237.7 cm^{-1} and 253.2 cm^{-1}, respectively, predicted theoretically based on data obtained with our EOM-CCSD/X2Cmmf/5Z* reference model. Given the weakly bound nature of the B^+ state,

TABLE II. Measured values $\tilde{\nu}_{v'7}$ of the observed $B^+(v') \leftarrow X^+(v'' = 7)$ transitions of $MgAr^+$ and the respective vibrational term values $T_{v'}$ and rotational constants $B_{v'}$ of the final states. All values are in cm^{-1}.

v'	$\tilde{\nu}_{v'7}$	$T_{v'}$	$B'_{v'}$	v'	$\tilde{\nu}_{v'7}$	$T_{v'}$	$B'_{v'}$
0	36 148.43(20)	0.00(28)	0.0608(10)	11	36 379.13(20)	230.70(28)	0.0324(10)
1	36 181.34(20)	32.91(28)	0.0550(20)	12	36 386.73(20)	238.30(28)	0.0293(10)
2	36 211.78(20)	63.35(28)	0.0543(10)	13	36 392.74(20)	244.31(28)	0.0212(10)
3	36 240.31(20)	91.88(28)	0.0521(10)	14	36 397.68(20)	249.25(28)	0.0203(10)
4	36 265.99(20)	117.56(28)	0.050[a]	15	36 401.25(20)	252.82(28)	0.0187(10)
5	36 289.44(20)	141.01(28)	0.048[a]	16	36 403.92(20)	255.49(28)	0.0190(20)
6	36 310.23(20)	161.80(28)	0.045[a]	17	36 405.95(40)	257.52(45)	0.013[b]
7	36 328.53(20)	180.10(28)	0.0420(10)	18	36 407.28(40)	258.85(45)	0.010[b]
8	36 344.53(20)	196.10(28)	0.0388(10)	19	36 407.80(40)	259.37(45)	0.007[b]
9	36 358.28(20)	209.85(28)	0.0359(10)	20	36 408.25(40)	259.82(45)	0.005[b]
10	36 369.52(20)	221.09(28)	0.0358(10)	21	36 408.85(40)	260.42(45)	0.005[b]

[a]Estimated by interpolation of the other measured rotational constants $B'_{v'}$.
[b]Estimated by extrapolation of the other measured rotational constants $B'_{v'}$.

additional diffuse basis functions might be required in the respective atomic basis sets for Mg and Ar to further improve the accuracy of our reference EOM-CCSD/X2Cmmf/5Z* model described in detail in Sec. III.

The vibrational bands with $v' \geq 17$ lie so close to each other that their rotational structures overlap. It is, therefore, not possible to assign rotational lines to specific vibrational bands in this range nor to use Eq. (10) to determine band origins and rotational constants. Instead, we estimated the rotational constants using a polynomial extrapolation of the values given in Table II and successively added the contributions of Hund's-case-(b)-to-Hund's-case-(c) transitions with an increase in the v' value to reproduce the experimental spectrum. In this process, the band origins were adjusted to give the best agreement between experiment and simulation, as given in Table II. Although the simulation allows the identification of a few individual rotational lines, we could not determine rotational constants of the final states with $v' \geq 17$ in this way because they are so small that the rotational structure of the spectra is essentially determined by the rotational constant of the initial state.

The data presented in Table II and in Figs. 4–6 provide a complete picture of all bound levels of the $MgAr^+$ B^+ state and form the basis for the global analysis of the $Mg(3p)Ar^+$ Rydberg complex discussed in Ref. 28.

B. Dissociation mechanisms

We have measured the TOF spectra associated with the KER and angular distributions of the dissociation products for the B^+ $v' = 0$–5, $v' = 8$–13 states and above the B^+ dissociation limit up to 36 700 cm^{-1}. All measurements were performed for parallel and perpendicular laser polarizations with respect to the TOF axis.

A selection of TOF spectra is presented in the upper panel of Fig. 7. In all TOF spectra that were recorded with the laser polarization parallel to the TOF axis, we observed two distinct peaks, which are well suited for the determination of the KER, whereas in the case of perpendicular polarization, the TOF distributions consisted of a single broad peak. In the remainder of this section, we focus the discussion on the spectra measured with the laser polarization parallel to the TOF axis, although similar considerations also apply to the spectra recorded with the polarization perpendicular to that axis. Starting from $v' = 0$ and up to $v' = 5$, one observes an increase in the separation Δt_{TOF} of the two peaks. At $v' = 8$, the TOF profiles abruptly change to a much narrower distribution, which broadens again for increasing vibrational levels. As the B^+ dissociation limit is crossed, one observes another sudden narrowing of the TOF distribution followed by a broadening as the wave number of the laser increases. These observations suggest that different dissociation mechanisms are at play in the three spectral regions (i) $v' = 0$–5, (ii) $v' = 8$–13, and (iii) above the dissociation limit. For each measured TOF spectrum, we determined the associated KER using the models described in Sec. II. In the regions (i) and (ii), the KERs were averaged over three independent measurements. The KERs are shown as a function of laser wave number in the lower panel of Fig. 7, in which the three regions described above are labeled with (i), (ii), and (iii). These regions are also depicted in the inset of Fig. 2.

In region (iii), direct photodissociation into the B^+ continuum takes place. The dissociation threshold $E_D(B^+ \leftarrow X^+(7)) = 36\,408.6(10)$ cm^{-1} of the B^+ state with respect to the $X^+(v'' = 7)$ state, shown as the dotted vertical line in Fig. 7, is accurately known from the analysis of the spectra presented in Paper II.[28] Therefore, the KER and, thus, the Mg^+ fragment velocity v are known accurately, and the measurements in region (iii) were used to calibrate the values of the model parameters t_0 and d_{TOF} in Eq. (4), which were not known accurately. The data points displayed in region (iii) correspond to the analysis using Eq. (6). Their linear extrapolation to zero KER (red dashed line) yields a dissociation threshold of $E_D = 36\,404.7(7)$ cm^{-1}, where the specified error does not include systematic errors but corresponds to the 1σ uncertainty of the extrapolation. The gap of data points around 36 480 cm^{-1} originates from the fact that the photodissociation cross section is too small in this range to record TOF spectra with a sufficient signal-to-noise ratio.

In region (ii), the TOF measurements were analyzed using Eq. (6) and the values of t_0 and d_{TOF} determined in region (iii).

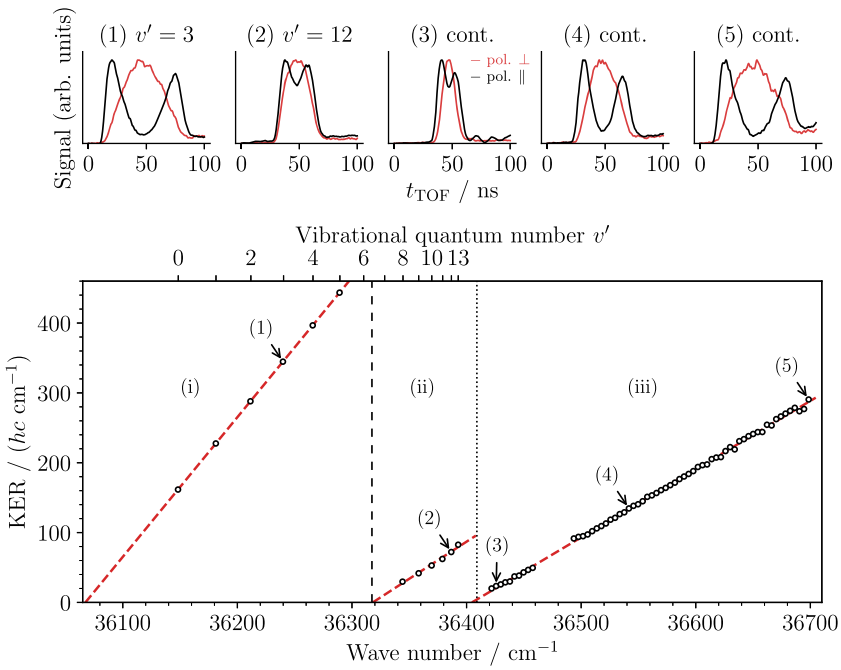

FIG. 7. Upper panels: typical TOF spectra recorded with laser polarization parallel (black) and perpendicular (red) to the TOF axis. The lower panel shows the KER determined from the TOF spectra as a function of the laser wave number, which suggests different dissociation mechanisms for the regions (i)–(iii). The vertical dashed line indicates the dissociation limit of the $A^+_{1/2}$ state, and the vertical dotted line indicates the dissociation limit of the B^+ state of $MgAr^+$. The labels (1)–(5) indicate the positions at which the TOF spectra presented in the upper panels were recorded.

The extrapolation of the KER to zero yielded a dissociation threshold with respect to the $X^+(v'' = 7)$ state of E_D = 36 318(2) cm^{-1}, where the specified error corresponds to an uncertainty of 1σ of the fit. This value is in good agreement with the $Mg^+(3p\ ^2P_{1/2}) + Ar(^1S_0)$ dissociation asymptote of the $A^+_{1/2}$ state, which lies at 36 317.0(10) cm^{-1}[28] and is shown as a vertical dashed line in Fig. 7. In region (ii), the $A^+_{1/2}$ dissociation continuum is accessible by predissociation from the $B^+(v')$ states through the nonadiabatic effects caused by the spin–orbit interaction. Hence, the predissociation has the same origin as the transition from Hund's case (b) to Hund's case (c) of the B^+ state discussed in Sec. IV A, namely, the mixing of the B^+ and $A^+_{1/2}$ states induced by the spin–orbit interaction.

In region (i), the TOF measurements were analyzed using Eq. (7). We first fitted the parameters a and b of Eq. (7) to Δt^2_{TOF} values measured in region (iii) and subsequently kept these parameters fixed to determine the dissociation threshold E_D from the KERs measured in region (i). The fit was only successful when assuming a two-photon dissociation, i.e., replacing $\tilde{\nu}_2$ by $2\tilde{\nu}_2$ in Eq. (7). The two-photon dissociation threshold with respect to the $X^+(v'' = 7)$ state was determined to be E_D = 72 135(5) cm^{-1} (the specified uncertainty corresponds to 1σ of the fit). This value is in good agreement with the expected positions of the $Mg^+(3d\ ^2D_{3/2,5/2}) + Ar(^1S_0)$ dissociation asymptotes at 72 138.8(10) cm^{-1} and 72 137.9(10) cm^{-1}, respectively, calculated using the cycle $E_D(B^+ \leftarrow X^+(7)) + E(Mg^+\ 3d\ ^2D_{3/2,5/2}) - E(Mg^+\ 3p\ ^2P_{3/2})$ and atomic term values from Ref. 46. The two-photon excitation, indicated by a dashed arrow in Fig. 2, takes place in the repulsive part of the $Mg(3d)Ar^+\ ^2\Sigma^+$ state and causes dissociation to the $Mg^+(3d\ ^2D_{3/2,5/2}) + Ar(^1S_0)$ asymptotes. In principle, two-photon dissociation is also possible in region (ii). However, in the TOF spectra we recorded, two-photon dissociation only gave rise to a broad and weak background, which suggests that the two-photon dissociation is much less efficient than predissociation at the laser intensities used to record the TOF spectra.

Our data, thus, unambiguously reveal three distinct dissociation mechanisms over a range of only ~300 cm^{-1}. In region (i), the molecules dissociate following two-photon resonance-enhanced absorption, producing Mg^+ ions in the 3d $^2D_{3/2,5/2}$ states. In region (ii), they predominantly predissociate into the $A^+_{1/2}$ continuum, producing Mg^+ ions in the 3p $^2P_{1/2}$ state. In region (iii), fragmentation occurs by direct photodissociation into the B^+ continuum, producing Mg^+ ions in the 3p $^2P_{3/2}$ state.

C. Dissociation dynamics and angular distributions

In the analysis of the TOF spectra presented in Fig. 7 for regions (ii) and (iii), we also obtained the values of the anisotropy parameter β, which are presented in Fig. 8. Figure 9 shows, as examples, the results of fits based on Eq. (6) to TOF spectra measured at the position of the predissociating $v' = 12$ level (36 386.6 cm^{-1}, left column) and above the dissociation threshold at 36 542.8 cm^{-1} (right column), respectively. The fits (dashed line) were performed using the spectra recorded with the laser polarized parallel to the TOF axis (upper panels). For $v' = 12$, we obtained a β value of 0.4, which is typical for the values we determined for predissociating states. In region (ii), the values of β were averaged over three independent measurements for each value of v' and varied between ~0.2 and ~0.5, with an average of 0.4, as shown on the left-hand side of Fig. 8.

In the continuum [region (iii)], we typically determined β values between ~1.4 and ~1.7 with an average of $\beta \approx 1.5$, as illustrated on the right-hand side of Fig. 8. The fit shown in the upper right

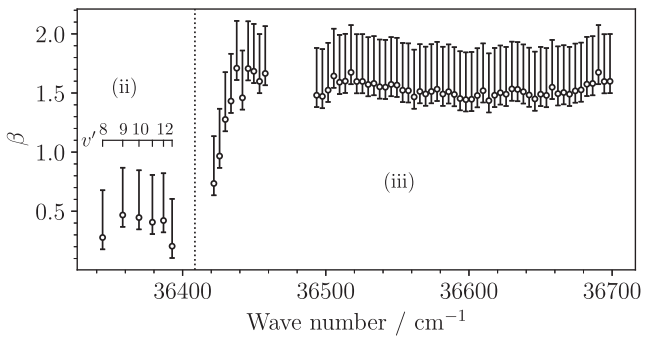

FIG. 8. Experimentally determined values of the anisotropy parameter β for regions (ii) and (iii) of the spectrum of the $B^+(v') \leftarrow X^+$ transition of $MgAr^+$. The markedly different values of β in the two regions originate from the different dissociation mechanisms that occur in these regions.

panel of Fig. 9 corresponds to the β value of 1.6. The origin of the rather different β parameters in regions (ii) and (iii) is discussed below. The spectra in the lower panels of Fig. 9 were recorded with the laser polarization perpendicular to the TOF axis under otherwise identical conditions, and the only parameter that was adjusted in the fit was the overall intensity I_0. The same β values, thus, adequately describe the measurements carried out with parallel and perpendicular polarization.

In direct dissociation, one approaches the axial-recoil limit, $\beta = 2$, for sufficiently low angular momenta and sufficiently high

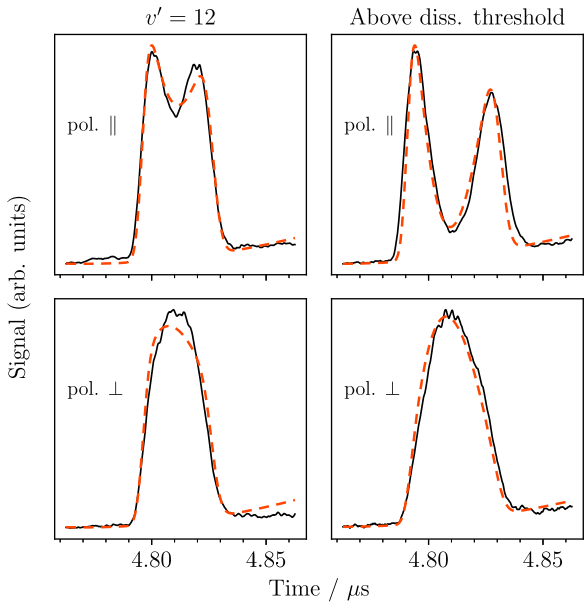

FIG. 9. Examples of TOF spectra observed following dissociation of $MgAr^+$ and the corresponding fits based on Eq. (6) (the dashed line) to determine the KER and β for $v' = 12$ and in the continuum at 36 542.8 cm^{-1}. The fit parameters for the cases where the laser was polarized perpendicular to the TOF axis (lower panels) are the same as for the cases where the laser was polarized parallel to the TOF axis (upper panels), except for an overall intensity factor. The fits in the left and right columns correspond to $\beta \approx 0.4$ and ~1.6, respectively.

KERs.[32] In the case of a $^1\Sigma$–$^1\Sigma$ transition, this limit corresponds to a difference $\delta_{N''+1} - \delta_{N''-1} = \pi$ of the phase shifts of the continuum nuclear wavefunctions accessed from a given initial-state rotational level with rotational quantum number N'' in the expression derived by Zare,[32]

$$\beta \approx \frac{2(N''^2 + N'' + 1) - 6N''(N'' + 1)\cos(\delta_{N''+1} - \delta_{N''-1})}{(2N'' + 1)^2}. \quad (11)$$

In the present case, we consider the transition between a $^2\Sigma$ state and a mixed $^2\Sigma_{1/2}$–$^2\Pi_{1/2}$ state, which has predominantly $^2\Sigma_{1/2}$ character in the relevant range of internuclear distances (see below). We, therefore, do not expect a strong deviation from $^1\Sigma$–$^1\Sigma$ photodissociation because of the weakly coupled nature of the electron spin. From the internuclear potential determined in Paper II,[28] we computed the phase shifts of the continuum wavefunctions using Numerov's method[51] and obtained the values of β by averaging them over the initial-state rotational distribution at 3 K. For a KER of 12 cm^{-1}, which corresponds to the lowest KER considered in the analysis of region (iii), we obtained $\beta = 1.88$. For higher KER, we calculated $\beta \gtrsim 1.9$, with monotonically increasing values of β for increasing KERs. At a KER of 300 cm^{-1}, corresponding to the highest KER considered in the analysis of region (iii), we obtained $\beta = 1.98$. The β values determined experimentally are systematically lower than the theoretical ones by about ~0.4. We attribute this discrepancy to the fact that our model for the TOF distributions does not perfectly reproduce the observed asymmetry between the two lobes of the distributions nor the position of the minimum between these lobes (see upper panels of Fig. 9). We, thus, believe that the fitted β values represent lower bounds of the actual values. The experimental values of β determined in the continuum (~1.5) are significantly higher than the value of 1.03 ± 0.05 determined at a KER corresponding to 580 cm^{-1} by Hoshino *et al.*[52]

The spin–orbit predissociation observed in the range from $v' = 7$ to the dissociation threshold [region (ii)] leads to a markedly different angular distribution of the fragments compared to direct dissociation, as reflected in the value of the measured anisotropy parameter $\beta \approx 0.4$. The fact that the rotational structure of the predissociative $B^+(v')$ states is partially resolved (see Fig. 6) indicates that predissociation broadening is smaller than the spacing of adjacent rotational energy levels. Classically, this means that the timescale associated with the rotational motion of the molecular ion is comparable to, or shorter than, the predissociation lifetime. The anisotropy of the angular distribution is expected to be reduced by the rotational motion compared to direct photodissociation in the axial-recoil approximation.[53] Moreover, the measured spectral lines do not exhibit asymmetric Fano profiles, indicating that direct photoexcitation to the dissociation continuum ($A^+_{1/2}$ in the present case) is negligible compared to excitation to levels of the B^+ state followed by predissociation. A more detailed analysis of the lifetimes of the predissociating states is presented in Paper II.[28]

Following a theoretical procedure similar to that introduced by Pernot *et al.*,[54] the β parameter associated with the excitation from a given $X^+(v'', N'')$ rovibrational level to a $B^+(v', J')$ predissociative level can be expressed within second-order perturbation theory as (see Appendix B)

$$\beta_{N''J'} = \frac{\sum_{J''} \beta_{J''J'} S(i\Lambda'' S'' N'' J''; e\Omega' J')}{\sum_{J''} S(i\Lambda'' S'' N'' J''; e\Omega' J')}. \quad (12)$$

In Eq. (12), $S(i\Lambda'' S'' N'' J''; e\Omega' J')$ is the transition line strength from a state described by Hund's coupling case (b), with a projection quantum number of the orbital angular momentum on the internuclear axis Λ'', a spin angular momentum quantum number S'', a total angular momentum quantum number without spin N'', a total angular momentum quantum number J'', and a set of other good quantum numbers *i*, to a predissociative state described by Hund's coupling case (c) with a total angular momentum quantum number J' and its projection quantum number Ω' onto the internuclear axis, and a set of other good quantum numbers *e*. The anisotropy parameters $\beta_{J''J'}$ associated with each $J' \leftarrow J''$ transitions are known analytically (see, e.g., Ref. 54) and tend to values of $\frac{1}{2}$ for $J' = J'' \pm 1$ (P and R branches) and -1 for $J' = J''$ (Q branch) in the limit of large J'' values. The total $\beta_{N''J'}$ parameter is, therefore, the weighted sum of the β parameters of the transitions from the various J'' sublevels of a given N'' level, with weights given by the relative strengths of the different branches.

The transition line strengths $S(i\Lambda'' S'' N'' J''; e\Omega' J')$ depend *a priori* on the extent of the $^2\Sigma_{1/2}$–$^2\Pi_{1/2}$ mixing in the upper state, caused by spin–orbit interaction and responsible for the Hund's-coupling-case-(c) nature of the high vibrational levels of the B^+ state. These case-(c) states, written as $|e\Omega' J' M'\rangle$, can be expanded in terms of case-(a) functions $|e\Lambda' S' \Sigma' \Omega' J' M'\rangle$ as

$$|ev'\Omega' J' M'\rangle = \sum_{\Lambda'} c_{\Lambda'}(R) |e\Lambda' S' \Sigma' \Omega' J' M'\rangle, \quad (13)$$

where Σ' is the projection quantum number of the spin on the internuclear axis and M' is the projection quantum number of the total angular momentum onto the *z* axis of the laboratory-fixed frame. The *R*-dependent expansion coefficients $c_{\Lambda'}(R)$ are obtained by diagonalization of the spin–orbit interaction matrix in the case (a) basis, as described in Paper II.[28] The transition line strengths $S(i\Lambda'' S'' N'' J''; e\Omega' J')$, thus, involve several vibronic transition moments of the form

$$\int dR\, c_{\Lambda'}(R) \chi^*_{\Lambda' v' J'}(R) M_{\Lambda'}(R) \chi_{v'' N''}(R), \quad (14)$$

where $\chi_{v'' N''}$ and $\chi_{\Lambda' v' J'}$ are the vibrational wave functions of the initial and predissociative states, respectively, and $M_{\Lambda'}(R)$ is the *R*-dependent electronic transition dipole moment. The vibrational wave function of the initial $X^+(v'' = 7)$ state considered in the present study has a non-negligible amplitude only in the range from $R \approx 4.5\ a_0$ to $R \approx 7.5\ a_0$. In this region, the Σ–Π mixing is very small in the B^+ state and, to a good approximation, $c_{\Lambda=0} = 1$ and $c_{|\Lambda|=1} = 0$. Therefore, the line strengths correspond to transitions from Hund's-coupling-case-(b) $^2\Sigma^+$ states to Hund's-coupling-case-(a) $^2\Sigma^+_{1/2}$ states, which can be calculated analytically.[55] In this way, the anisotropy parameter $\beta_{N''J'}$ can be calculated for arbitrary N'' and J' values.

The experimental β parameter for the $v' = 12$ vibrational band was recorded at a wave number of 36 386.60 cm^{-1}. Three rotational transitions lie within the 0.1 cm^{-1} laser bandwidth, and the experimental result corresponds to the sum of the three individual $\beta_{N''J'}$ values (0.71, 0, and 0.70, respectively, in the order of increasing wave number) weighted by the product of the corresponding line intensities with the spectral intensity of the laser light at the transition wave numbers (0.14, 0.16, and 0.70, respectively). The total calculated β parameter is 0.58, in reasonable agreement with the experimental value of ~0.4. A β parameter of 0.5 is expected for high J' values (see above). However, for the low J' values considered in the present case, this argument is not valid, and the origin of the $\beta = 0.5$ value lies rather in the dynamic averaging caused by the overlapping rotational transitions. A similar agreement between the measured and calculated anisotropy parameters was obtained for the $v' = 8$–13 predissociating states.

D. Intensities of the vibronic transitions

Panels (a) and (b) in Fig. 10 present overview spectra of the $B^+ \leftarrow X^+(v'' = 7)$ transition extending from $v' = 0$ up to ~300 cm^{-1}

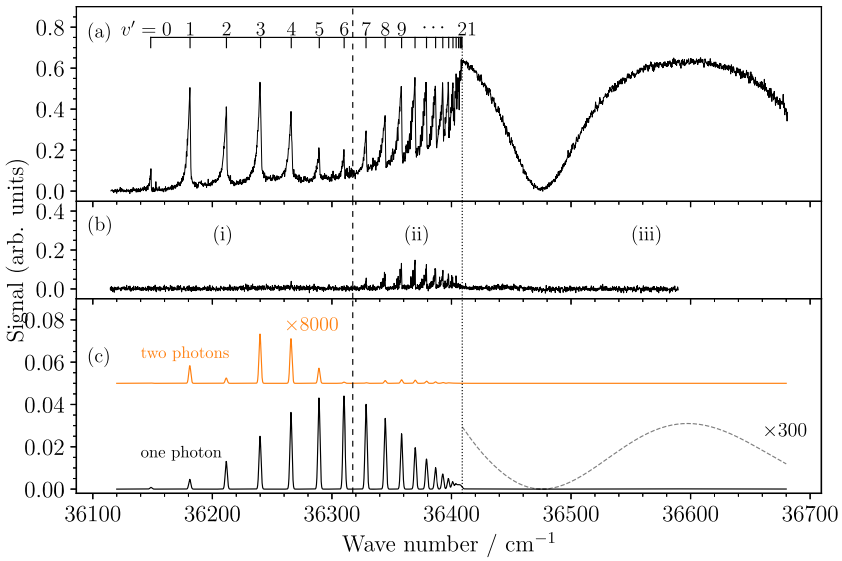

FIG. 10. Panels (a) and (b): overview spectra of the $B^+(v') \leftarrow X^+(v'' = 7)$ transition of $MgAr^+$ recorded at laser pulse energies of ~0.5 mJ and <1 μJ, respectively. Panel (c): two-photon (upper trace) and one-photon (lower trace) Franck–Condon factors, after convolution with a Gaussian line shape function with a FWHM of 2 cm^{-1}. The Franck–Condon factors of the two-photon transitions and the single-photon transition to the B^+ continuum (dashed curve) were scaled by 8000 and 300, respectively, to be visible on the scale of the figure (see text for details).

above the dissociation threshold, recorded with laser pulse energies of ~0.5 mJ and <1 μJ, respectively. We refer to them below as the high-intensity and low-intensity spectra, respectively. In the regions designated as (i)–(iii) in Fig. 10, which are the same as in Fig. 7, these spectra exhibit very different patterns.

The high-intensity spectrum in regions (i) and (ii) in Fig. 10(a) is the same as in Fig. 4 and exhibits an intensity minimum around $v' = 6$. The continuum region [region (iii)] in Fig. 10(a), i.e., above 36 409 cm^{-1}, reveals an intensity minimum around 36 480 cm^{-1} and a broad maximum around 36 600 cm^{-1}. The low-intensity spectrum, presented in Fig. 10(b), only possesses nonzero intensity in region (ii).

The intensity patterns apparent in panels (a) and (b) of Fig. 10 can be explained with the dissociation mechanisms described in Sec. IV B when considering the Franck–Condon factors of the corresponding transitions. We have determined these factors using the potential of the X^+ state published in Ref. 29, the potential of the B^+ state reported in Paper II,[28] and the potential of the Mg(3d)Ar^+ $^2\Sigma^+$ state calculated *ab initio*, as described in Sec. III (see also Fig. 2). The vibrational wavefunctions were calculated by solving the nuclear Schrödinger equation using a Legendre–Gauss–Lobatto discrete-variable-representation technique in combination with exterior complex scaling (ECS).[28,29,56–58] The Franck–Condon factors of the $B^+ \leftarrow X^+$ one-photon transition and the Mg(3d)Ar^+ $^2\Sigma^+ \leftarrow B^+ \leftarrow X^+$ resonant two-photon transition are shown in Fig. 10(c) as black and orange curves, respectively, after convolution with a Gaussian line shape function with a FWHM of 2 cm^{-1}. In the latter case, the Franck–Condon factors represent products of the Franck–Condon factor of the $B^+ \leftarrow X^+$ transition and the Franck–Condon factor of the Mg(3d)Ar^+ $^2\Sigma^+ \leftarrow B^+$ bound-to-continuum transition determined as explained in Appendix C. To account for the very different efficiencies of the different excitation processes, the Franck–Condon factors of the two-photon transitions and the direct dissociation [region (iii)] had to be enhanced by factors of 8000 and 300, respectively, compared to the one-photon transitions to the predissociative levels of the B^+ state. This analysis confirms that the high-intensity spectrum in panel (a) was recorded under saturating conditions.

In region (i), the Franck–Condon factors calculated for the resonant two-photon transitions suggest that two-photon dissociation is much more efficient in this region than in regions (ii) and (iii), as discussed in Sec. IV B. Moreover, they qualitatively reproduce the drop in intensity toward $v' = 6$ observed in the high-intensity spectrum [Fig. 10(a)] and the weaker intensity of the transition to $v' = 2$.

In region (ii), the relative intensities of the observed lines are not well described by the calculated Franck–Condon factors of the $B^+ \leftarrow X^+$ transition (black curve). In the case of the high-intensity spectrum [Fig. 10(a)], we attribute the constant intensities of transitions to the highest vibrational levels to the saturation of the transitions, whereas the relative intensities measured in the low-intensity spectrum are governed by the predissociation dynamics. Except for $v' = 7$, the calculated predissociation widths also support this finding (see supplementary material in Paper II[28]). The fact that we observe a signal in region (ii) but not in region (i) at low intensities is another indication of the proposed one- and two-photon dissociation mechanisms, respectively.

The high-intensity spectrum [Fig. 10(a)] exhibits stronger maximal intensities in region (iii) than in region (ii). Moreover, the lobe around 36 600 cm^{-1} is significantly broader than predicted by the Franck–Condon analysis. This behavior can also be explained by saturation. Whereas in region (ii), the populations of the initial and final states equilibrate, in region (iii), the entire initial-state population yield may be drained into the photodissociation continuum, which leads to a higher Mg^+ yield. As described in Paper II,[28] the spectrum in region (iii) was used to optimize the repulsive part of the B^+ potential curve such that the calculated positions of the intensity minimum and maximum matched the positions observed experimentally. In the low-intensity spectrum [Fig. 10(b)], no dissociation products were observed in region (iii), as expected from the low Franck–Condon factors.

V. CONCLUSIONS AND OUTLOOK

In this article, we have reported on the first step of a systematic investigation of the Rydberg states of a molecular cation, $MgAr^+$, which consisted in the observation and full characterization of the B^+ $^2\Sigma^+$ state of $MgAr^+$ located below the $Mg^+(3p\,^2P_{3/2}) + Ar(^1S_0)$ dissociation threshold. This state and the two spin–orbit components ($\Omega = 1/2$ and 3/2) of the A^+ $^2\Pi_\Omega$ state of $MgAr^+$ form a low-lying 3p Rydberg complex, which can be regarded as the first stepping stone toward ionization[12] of $MgAr^+$ and the formation of the doubly charged ion $MgAr^{2+}$. Whereas previous theoretical work had emphasized the repulsive nature of the B^+ state at short range,[21] new *ab initio* calculations carried out in the realm of the present investigation indicated a potential well at long range ($R_e \approx 4.4$ Å) able to support several vibrational levels.

Using the method of isolated-core (multi)photon Rydberg-dissociation spectroscopy,[27] we have recorded rotationally resolved spectra of transitions from the selected $X^+(v'' = 7)$ state of $MgAr^+$ to all vibrational levels of the B^+ state from $v' = 0$–21, from which we have extracted an extensive set of molecular constants. The rotational structure of the vibrational levels of the B^+ state undergoes a transition from Hund's angular-momentum coupling case (b) at low v' values to case (c) at high v' values, which we attribute to a mixing of the B^+ and $A^+_{1/2}$ states at large internuclear distances induced by the spin–orbit interaction.

We have also identified the mechanisms through which high Rydberg states of Mg are produced following photodissociation of the isolated state-selected $MgAr^+$ ion core by measuring the kinetic-energy release upon dissociation and the corresponding β parameters. These mechanisms include (i) resonant two-photon dissociation, via the lowest vibrational levels of the B^+ state, to the $Mg^+(3d\,^2D_{3/2,5/2}) + Ar(^1S_0)$ dissociation continua accessed through the repulsive branch of the potential of the $^2\Sigma^+$ state of the 3d complex; (ii) predissociation of the vibrational levels of the B^+ state with $v' \geq 7$ to the $Mg^+(3p\,^2P_{1/2}) + Ar(^1S_0)$ dissociation continuum mediated by the spin–orbit interaction; and (iii) direct photodissociation to the $Mg^+(3p\,^2P_{3/2}) + Ar(^1S_0)$ continuum of the B^+ state. Finally, we have observed a broad intensity oscillation in the photodissociation continuum of the B^+ state, which we have quantitatively interpreted in terms of Franck–Condon densities for bound–continuum transitions (see Appendix C).

In the next steps of this investigation, we intend to present a global model of the 3p Rydberg complex of $MgAr^+$[28] and the analysis

of isolated-core Rydberg-dissociation spectra in the region of the 3d and 4s complexes.

ACKNOWLEDGMENTS

The authors would like to thank J. A. Agner and H. Schmutz for technical support. This work was supported financially by the Swiss National Science Foundation (Grant No. 200020-172620) and the European Research Council through an advanced grant under the European Union's Horizon 2020 research and innovation program (Grant No. 743121).

APPENDIX A: DETAILS OF THE ANALYSIS OF THE TOF DISTRIBUTIONS

In this section, we provide the details of the derivation and application of Eq. (6). In order to apply Eq. (5) to analyze TOF distributions recorded with a linear TOF spectrometer, one needs to perform two subsequent changes of variables, namely, $\theta \rightarrow z$ and $z \rightarrow t_{\mathrm{TOF}}$. The first transformation involves the integration over the azimuthal angle around the z axis and depends on the laser polarization. We discuss the cases $\theta_z = \theta$ (polarization parallel to the z axis) and $\theta_z = \theta + \pi/2$ (polarization perpendicular to the z axis) separately.

$\theta_z = \theta$: In the case of parallel polarization, we have $z - z_0' = r\cos\theta$ and the surface element is $\mathrm{d}z\mathrm{d}\phi_z/r$, where $r = \Delta t_{\mathrm{prep}} v$ and ϕ_z is the azimuthal angle of the angular distribution, which coincides with the azimuthal angle around the z axis. The angular distribution as a function of z can then be obtained by

$$\begin{aligned}\mathrm{d}I(z) &= \int_0^{2\pi} \frac{I_0}{4\pi r}\left[1+\beta P_2((z-z_0')/r)\right]\mathrm{d}z\mathrm{d}\phi_z \\ &= \frac{I_0}{2r}\left[1+\beta P_2((z-z_0')/r)\right]\mathrm{d}z. \end{aligned} \tag{A1}$$

$\theta_z = \theta + \pi/2$: In the case of perpendicular polarization, we have $\cos\theta = \sqrt{r^2-(z-z_0)^2}/r \sin\phi_z$ and the surface element is again $\mathrm{d}z\mathrm{d}\phi_z/r$. Integration over ϕ_z yields

$$\begin{aligned}\mathrm{d}I(z) &= \frac{I_0}{4\pi r}\int_0^{2\pi}\left[1+\beta P_2\left(\frac{\sqrt{r^2-(z-z_0')^2}}{r}\sin\phi_z\right)\right]\mathrm{d}z\mathrm{d}\phi_z \\ &= \frac{I_0}{2r}\left[1-\frac{\beta}{2}P_2((z-z_0')/r)\right]\mathrm{d}z, \end{aligned} \tag{A2}$$

which is identical to Eq. (A1) after replacing β by $-\beta/2$.

Inversion of Eq. (4) yields the required dependence of z on t_{TOF} for the second change of variables,

$$z(t_{\mathrm{TOF}}) = \frac{\left(bt_{\mathrm{TOF}}^2 - 4d_{\mathrm{TOF}}\right) \pm \sqrt{\left(bt_{\mathrm{TOF}}^2 - 4d_{\mathrm{TOF}}\right)^2 - 16d_{\mathrm{TOF}}^2}}{8}, \tag{A3}$$

where $b = 2qF/m_{\mathrm{Mg}}$. The choice of sign in Eq. (A3) depends on how far the cloud of dissociation products extends within the electrode stack. If the dissociation products exceed $z = d_{\mathrm{TOF}}/2$, one has to make a careful distinction between particles for which $z < d_{\mathrm{TOF}}/2$ and particles for which $z > d_{\mathrm{TOF}}/2$. In the present experiments, the condition $z < d_{\mathrm{TOF}}/2$ was always fulfilled, and thus, only the negative sign in Eq. (A3) was relevant. Using

$$\mathrm{d}z = \left|\frac{\mathrm{d}z}{\mathrm{d}t_{\mathrm{TOF}}}\right|\mathrm{d}t_{\mathrm{TOF}}, \tag{A4}$$

one obtains Eq. (6) from Eqs. (A1), (A3), and (A4).

Because the molecules occupy a finite volume rather than a single point z_0', one has to take into account the initial distribution of photoexcited molecules by computing the weighted sum,

$$\mathrm{d}I(t_{\mathrm{TOF}}) = \int \mathrm{d}I(t_{\mathrm{TOF}}, z_0')p(z_0')\mathrm{d}z_0', \tag{A5}$$

for each value of t_{TOF}. In Eq. (A5), $p(z_0')$ is the distribution of dissociating molecules, which is governed by the laser profile and is well described by a Gaussian distribution in our experiment.

APPENDIX B: PREDISSOCIATION ANGULAR DISTRIBUTION

The angular distribution of fragments following predissociation of a diatomic molecule has been investigated by a number of authors.[33,53,54,59–61] We follow here an approach similar to those of Mukamel and Jortner[59] and Pernot *et al.*,[54] which we adapted to the present case. We consider the transition from an initial state described by Hund's coupling case (b) to a final state described by Hund's coupling case (c) via a predissociative state also described by Hund's coupling case (c). The initial state is denoted by $|i\Lambda''S''N''J''M''\rangle$ and has an energy $E_{iN''}$. The final state is denoted by $|d\Omega\boldsymbol{k}\rangle$, where $\boldsymbol{k}$ is the momentum vector of the fragments corresponding to a KER of $\mu k^2/2$. The predissociative state is denoted by $|e\Omega'J'M'\rangle$ and has the energy $E_{eJ'}$ and a predissociation rate $\Gamma_{eJ'}$. All wave functions are expressed within the Born–Oppenheimer approximation. Within lowest-order perturbation theory and neglecting direct excitation to the dissociation continuum, the differential cross section $\frac{\mathrm{d}\sigma}{\mathrm{d}\Omega}$ for photodissociation by a photon with energy $\hbar\omega$ can be written as[59]

$$\begin{aligned}\frac{\mathrm{d}\sigma}{\mathrm{d}\Omega} &= \frac{(2\pi)^2}{\hbar c} \\ &\times \left|\sum_{eJ'M'}\frac{\langle d\Omega\boldsymbol{k}|H_v|e\Omega'J'M'\rangle\langle e\Omega'J'M'|\hat{\epsilon}\cdot\boldsymbol{\mu}|i\Lambda''S''N''J''M''\rangle}{E_{iN''}+\hbar\omega-E_{eJ'}+\frac{\mathrm{i}}{2}\Gamma_{eJ'}}\right|^2. \end{aligned} \tag{B1}$$

The operator H_v represents the coupling of the intermediate state to the dissociation continuum and will be left unspecified in the following for the sake of generality. In the present case, it represents the non-adiabatic spin–orbit coupling between the B^+ and $A^+_{1/2}$ states responsible for spin–orbit predissociation. $\hat{\epsilon}\cdot\boldsymbol{\mu}$ is the electric-dipole transition operator.

Expression (B1) can be simplified in several ways. First, we write the continuum wave function as a partial-wave expansion,[32]

$$\langle d\Omega\boldsymbol{k}| = \sum_{JM}(2J+1)^{1/2}\mathrm{i}^J\mathrm{e}^{-\mathrm{i}\delta_J}D^J_{M\Omega}(\phi,\theta,0)\,\langle dk\Omega JM|, \tag{B2}$$

where ϕ, θ are the angles between the vectors $\hat{\epsilon}$ and $\boldsymbol{k}$, $D^J_{M\Omega}$ represents a Wigner rotation matrix, and δ_J is the scattering phase shift. The total angular momentum quantum number J' of the intermediate state and its projection quantum number M' are conserved upon predissociation. Moreover, since predissociation is unaffected by the orientation of the molecular ion in the lab-fixed frame, the corresponding matrix element should be independent of M'. We combine

these two properties by writing

$$\langle dk\Omega JM|H_v|e\Omega' J'M'\rangle = R^{J'}_{e\Omega',dk\Omega}\delta_{J'J}\delta_{M'M}. \tag{B3}$$

In a second step, we assume that the broadening of the transition resulting from predissociation (full width at half maximum $\Gamma_{ej'}$) is significantly smaller than the energy spacing between adjacent rotational levels so that the rotational structure of the intermediate state can be resolved. Therefore, when the photon energy is resonant with a transition, only the term associated with this transition contributes significantly to the sum in Eq. (B1), and other off-resonant terms can be neglected.

In a third step, we rewrite the squared norm of the transition dipole matrix element in terms of the transition line strength $S(i\mathcal{N}''; ej')$, giving

$$\begin{aligned}&\left|\langle e\Omega' J'M'|\hat{\epsilon}\cdot\boldsymbol{\mu}|i\Lambda''S''N''J''M''\rangle\right|^2\\ &\quad=\begin{pmatrix} J' & 1 & J'' \\ -M' & 0 & M''\end{pmatrix}^2 S(i\Lambda''S''N''J'';e\Omega'J')\end{aligned} \tag{B4}$$

in the case of linear polarization. Equation (B1) can now be rewritten as

$$\begin{aligned}\frac{d\sigma}{d\Omega} &= \frac{(2\pi)^2}{\hbar c}\frac{(2J'+1)\left|R^{J'}_{e\Omega' d\Omega}\right|^2}{(E_{i\mathcal{N}''}+\hbar\omega-E_{ej'})^2+\left(\frac{\Gamma_{ej'}}{2}\right)^2}\\ &\times S(i\Lambda''S''N''J'';e\Omega'J')\\ &\times\begin{pmatrix} J' & 1 & J'' \\ -M'' & 0 & M''\end{pmatrix}^2\left|D^{J'}_{M''\Omega}(\phi,\theta,0)\right|^2,\end{aligned} \tag{B5}$$

where we used the fact that $M' = M''$ for a dipole transition with linear polarization along the z axis of the laboratory frame.

The total differential cross section is obtained by summing over the relevant initial and final states. In the present case, there are two dissociation continua with $\Omega = \pm 1/2$. We use the fact that the squared norm of the Wigner D matrix in Eq. (B5) is independent of the sign of Ω.[62] Moreover, Fermi's golden rule allows one to relate the predissociation matrix element $R^{J'}_{e\Omega' d\Omega}$ to the predissociation rate $\Gamma_{ej'}$,

$$\sum_{\Omega=-1/2}^{1/2}\left|R^{J'}_{e\Omega' d\Omega}\right|^2 = \frac{\Gamma_{ej'}}{2\pi}. \tag{B6}$$

Finally, we assume that all degenerate levels associated with the initial ground state are equally populated. This leads to

$$\begin{aligned}\frac{d\sigma}{d\Omega} &= \frac{(2\pi)^2}{\hbar c}\frac{(2J'+1)}{(2S''+1)(2N''+1)}\\ &\times\frac{1}{\pi}\frac{\frac{1}{2}\Gamma_{ej'}}{(E_{i\mathcal{N}''}+\hbar\omega-E_{ej'})^2+\left(\frac{\Gamma_{ej'}}{2}\right)^2}\\ &\times\sum_{J''=|N''-S''|}^{N''+S''} S(i\Lambda''S''N''J'';e\Omega'J')\\ &\times\sum_{M''}\begin{pmatrix} J' & 1 & J'' \\ -M'' & 0 & M''\end{pmatrix}^2\left|d^{J'}_{M''|\Omega|}(\theta)\right|^2,\end{aligned} \tag{B7}$$

where $d^{J'}_{M''|\Omega|}$ is a small-d Wigner matrix. The sum over M'' on the right-hand side of the above equation is known analytically and can be written as $\frac{1}{2}(1+\beta_{J'J''}P_2(\cos\theta))$. The corresponding formulas for $\beta_{J''J'}$ have been tabulated by Zare[63] (see also the work of Pernot *et al.*[54]). Other terms on the right-hand side of Eq. (B7) include the ratio between the degeneracies of the final and initial states, a Lorentzian function describing the transition line shape, and a sum of the angular distribution of all degenerate J'' levels belonging to a given N'', weighted by the respective line strengths. Equation (12) can be obtained from Eq. (B7).

APPENDIX C: CALCULATION OF THE FRANCK–CONDON FACTORS

The Franck–Condon factors f_{bb} of transitions between bound states presented in Fig. 10(c) were calculated in the usual way as

$$f_{\mathrm{bb}} = \langle v'|v''\rangle^2, \tag{C1}$$

where $|v''\rangle$ and $|v'\rangle$ correspond to the vibrational wavefunctions of the initial and final states, respectively, obtained by solving the nuclear Schrödinger equation. For transitions to continuum states, we computed the Franck–Condon density,[64]

$$f\frac{df}{d\tilde{\nu}}(\tilde{\nu}) = \langle\tilde{\nu}|v''\rangle^2, \tag{C2}$$

where we label the energy-normalized continuum state $|\tilde{\nu}\rangle$ with the transition wave number $\tilde{\nu}$. Although the expressions in Eqs. (C1) and (C2) are widely used to discuss transition intensities, they do not allow for a direct comparison of transition probabilities to bound states and continuum states because of their different meaning. To obtain the Franck–Condon factors of transitions to continuum states that are directly comparable with Eq. (C1), we integrated the Franck–Condon density over the bandwidth of the laser radiation responsible for photodissociation,

$$f_{\mathrm{bc}}(\tilde{\nu}_{\mathrm{L}}) = \frac{1}{\tilde{I}_0}\int\frac{df}{d\tilde{\nu}}(\tilde{\nu})\tilde{I}(\tilde{\nu})d\tilde{\nu}. \tag{C3}$$

In Eq. (C3), $\tilde{I}(\tilde{\nu})$ is the laser spectral intensity distribution, $\tilde{I}_0$ is the maximum laser spectral intensity, and $\tilde{\nu}_{\mathrm{L}}$ is the corresponding central wave number. Continuum Franck–Condon factors f_{bc}, thus, depend on experimental conditions. Assuming that the laser spectral intensity is well described by a Gaussian function and the Franck–Condon density is approximately constant over the laser bandwidth $\Delta\tilde{\nu}$, the integral can be approximated by

$$f_{\mathrm{bc}}(\tilde{\nu}_{\mathrm{L}}) \approx \frac{1}{\tilde{I}_0}\frac{df}{d\tilde{\nu}}(\tilde{\nu}_{\mathrm{L}})\int\tilde{I}(\tilde{\nu})d\tilde{\nu} = \frac{\sqrt{\pi}\Delta\tilde{\nu}}{2\sqrt{\ln 2}}\frac{df}{d\tilde{\nu}}(\tilde{\nu}_{\mathrm{L}}). \tag{C4}$$

In our calculations, we used exterior complex scaling (ECS)[28,58] to compute the continuum solutions of the nuclear Schrödinger equation. Within the framework of ECS, the Franck–Condon density can be computed as[65]

$$\frac{df}{d\tilde{\nu}}(\tilde{\nu}) = \frac{1}{\pi}\mathrm{Im}\sum_{v_\theta}\frac{\langle v_\theta|v''\rangle^2}{E_{v_\theta}-E_{v''}-hc\tilde{\nu}}, \tag{C5}$$

which is a continuous function of $\tilde{\nu}$. In Eq. (C5), θ designates the complex-rotation angle, $E_{v''}$ denotes the energy eigenvalue of the initial state, and E_{v_θ} is the complex energy eigenvalue of the

continuum state $|v_\theta\rangle$. The Franck–Condon factors of the $B^+(v') \leftarrow X^+(v'' = 7)$ transitions were calculated using Eqs. (C1) and (C4) for the bound–bound [regions (i) and (ii)] and the bound–continuum transitions [region (iii)], respectively. The Franck–Condon factors $f_{2p}(\tilde{\nu}_{v'v''})$ of the resonant $Mg(3d)Ar^+\,^2\Sigma^+ \leftarrow B^+(v') \leftarrow X^+(v'' = 7)$ two-photon transitions were calculated as products of the bound–bound Franck–Condon factor $\langle v'|v''\rangle^2$ for the first excitation step and the bound–continuum Franck–Condon factor defined in Eq. (C4) for the second, dissociative transition, i.e.,

$$f_{2p}(\tilde{\nu}_{v'v''}) = \langle v'|v''\rangle^2 \cdot \frac{\sqrt{\pi}\Delta\tilde{\nu}}{2\sqrt{\ln 2}} \frac{df}{d\tilde{\nu}}(\tilde{\nu}_{v'v''}), \tag{C6}$$

where $\Delta\tilde{\nu} = 0.1\ cm^{-1}$ in our experiment.

DATA AVAILABILITY

The data that support the findings of this study are available from the corresponding author upon reasonable request.

REFERENCES

[1] J. P. Maier, Int. J. Mass Spectrom. Ion Processes **104**, 1 (1991).
[2] L. Zhu and P. Johnson, J. Chem. Phys. **94**, 5769 (1991).
[3] K. Müller-Dethlefs and E. W. Schlag, Angew. Chem., Int. Ed. Engl. **37**, 1346 (1998).
[4] M. A. Duncan, Int. J. Mass Spectrom. **200**, 545 (2000).
[5] T. Oka, *The Encyclopedia of Mass Spectrometry* (Elsevier, Amsterdam, 2003), Vol. 1, p. 217.
[6] S. K. Stephenson and R. J. Saykally, Chem. Rev. **105**, 3220 (2005).
[7] T. Amano, in *Handbook of High-Resolution Spectroscopy*, edited by M. Quack and F. Merkt (John Wiley & Sons, Chichester, 2011), pp. 1267–1289.
[8] S. Willitsch, in *Handbook of High-Resolution Spectroscopy*, edited by M. Quack and F. Merkt (John Wiley & Sons, Chichester, 2011), pp. 1691–1712.
[9] F. Merkt, S. Willitsch, and U. Hollenstein, in *Handbook of High-Resolution Spectroscopy*, edited by M. Quack and F. Merkt (John Wiley & Sons, Chichester, 2011), Vol. 3, pp. 1617–1654.
[10] S. Brünken, L. Kluge, A. Stoffels, J. Pérez-Ríos, and S. Schlemmer, J. Mol. Spectrosc. **332**, 67 (2017).
[11] D. Schröder and H. Schwarz, J. Phys. Chem. A **103**, 7385 (1999).
[12] R. S. Mulliken, J. Am. Chem. Soc. **86**, 3183 (1964).
[13] I. Velchev, W. Hogervorst, and W. Ubachs, J. Phys. B: At., Mol. Opt. Phys. **32**, L511 (1999).
[14] M. Génévriez, D. Wehrli, J. A. Agner, and F. Merkt, Int. J. Mass Spectrom. **435**, 209 (2019).
[15] H. Partridge, C. W. Bauschlicher, and S. R. Langhoff, J. Phys. Chem. **96**, 5350 (1992).
[16] R. J. Le Roy, J. Chem. Phys. **101**, 10217 (1994).
[17] C. W. Bauschlicher, Jr. and H. Partridge, Chem. Phys. Lett. **239**, 241 (1995).
[18] K. L. Burns, D. Bellert, A. W.-K. Leung, and W. H. Breckenridge, J. Chem. Phys. **114**, 7877 (2001).
[19] D. Bellert and W. H. Breckenridge, Chem. Rev. **102**, 1595 (2002).
[20] A. M. Gardner, C. D. Withers, J. B. Graneek, T. G. Wright, L. A. Viehland, and W. H. Breckenridge, J. Phys. Chem. A **114**, 7631 (2010).
[21] W. Gaied, H. Habli, B. Oujia, and F. X. Gadea, Eur. Phys. J. D **62**, 371 (2011).
[22] W. D. Tuttle, J. P. Harris, Y. Zheng, W. H. Breckenridge, and T. G. Wright, J. Phys. Chem. A **122**, 7679 (2018).
[23] J. S. Pilgrim, C. S. Yeh, and M. A. Duncan, Chem. Phys. Lett. **210**, 322 (1993).
[24] J. S. Pilgrim, C. S. Yeh, K. R. Berry, and M. A. Duncan, J. Chem. Phys. **100**, 7945 (1994).
[25] C. S. Yeh, J. S. Pilgrim, K. F. Willey, D. L. Robbins, and M. A. Duncan, Int. Rev. Phys. Chem. **13**, 231 (1994).
[26] C. T. Scurlock, J. S. Pilgrim, and M. A. Duncan, J. Chem. Phys. **103**, 3293 (1995).
[27] M. Génévriez, D. Wehrli, and F. Merkt, Mol. Phys. **118**, e1703051 (2020).
[28] M. Génévriez, D. Wehrli, and F. Merkt, J. Chem. Phys. **153**, 074311 (2020).
[29] D. Wehrli, M. Génévriez, C. Kreis, J. A. Agner, and F. Merkt, J. Phys. Chem. A **124**, 379 (2020).
[30] R. R. Bennett, J. G. McCaffrey, and W. H. Breckenridge, J. Chem. Phys. **92**, 2740 (1990).
[31] R. R. Bennett, J. G. McCaffrey, I. Wallace, D. J. Funk, A. Kowalski, and W. H. Breckenridge, J. Chem. Phys. **90**, 2139 (1989).
[32] R. N. Zare, Mol. Photochem. **4**, 1 (1972).
[33] R. N. Dixon, J. Chem. Phys. **122**, 194302 (2005).
[34] A. Shee, T. Saue, L. Visscher, and A. S. P. Gomes, J. Chem. Phys. **149**, 174113 (2018).
[35] T. Fleig, J. Olsen, and L. Visscher, J. Chem. Phys. **119**, 2963 (2003).
[36] S. Knecht, H. J. A. Jensen, and T. Fleig, J. Chem. Phys. **132**, 014108 (2010).
[37] S. Knecht, Ö. Legeza, and M. Reiher, J. Chem. Phys. **140**, 041101 (2014).
[38] S. Battaglia, S. Keller, and S. Knecht, J. Chem. Theory Comput. **14**, 2353 (2018).
[39] T. H. Dunning, Jr., J. Chem. Phys. **90**, 1007 (1989).
[40] J. Thyssen, "Development and applications of methods for correlated relativistic calculations of molecular properties," Ph.D. dissertation (Department of Chemistry, University of Southern Denmark, 2001).
[41] J. Sikkema, L. Visscher, T. Saue, and M. Iliaš, J. Chem. Phys. **131**, 124116 (2009).
[42] DIRAC, a relativistic *ab initio* electronic structure program, Release DIRAC19, 2019, written by A. S. P. Gomes, T. Saue, L. Visscher, H. J. Aa. Jensen, and R. Bast, with contributions from I. A. Aucar, V. Bakken, K. G. Dyall, S. Dubillard, U. Ekström, E. Eliav, T. Enevoldsen, E. Faßhauer, T. Fleig, O. Fossgaard, L. Halbert, E. D. Hedegård, B. Heimlich–Paris, T. Helgaker, J. Henriksson, M. Iliaš, Ch. R. Jacob, S. Knecht, S. Komorovský, O. Kullie, J. K. Lærdahl, C. V. Larsen, Y. S. Lee, H. S. Nataraj, M. K. Nayak, P. Norman, G. Olejniczak, J. Olsen, J. M. H. Olsen, Y. C. Park, J. K. Pedersen, M. Pernpointner, R. di Remigio, K. Ruud, P. Sałek, B. Schimmelpfennig, B. Senjean, A. Shee, J. Sikkema, A. J. Thorvaldsen, J. Thyssen, J. van Stralen, M. L. Vidal, S. Villaume, O. Visser, T. Winther, and S. Yamamoto, Zenodo. https://doi.org/10.5281/zenodo.3572669, see also http://www.diracprogram.org.
[43] T. Saue, R. Bast, A. S. P. Gomes, H. J. A. Jensen, L. Visscher, I. A. Aucar, R. di Remigio, K. G. Dyall, E. Eliav, E. Fasshauer, T. Fleig, L. Halbert, E. D. Hedegård, B. Helmich-Paris, M. Iliaš, C. R. Jacob, S. Knecht, J. K. Laerdahl, M. L. Vidal, M. K. Nayak, M. Olejniczak, J. M. H. Olsen, M. Pernpointner, B. Senjean, A. Shee, A. Sunaga, and J. N. P. van Stralen, J. Chem. Phys. **152**, 204104 (2020).
[44] S. Keller, M. Dolfi, M. Troyer, and M. Reiher, J. Chem. Phys. **143**, 244118 (2015).
[45] S. Knecht, E. D. Hedegård, S. Keller, A. Kovyrshin, Y. Ma, A. Muolo, C. J. Stein, and M. Reiher, Chimia **70**, 244 (2016).
[46] A. Kramida, Yu. Ralchenko, J. Reader, and NIST ASD Team, NIST Atomic Spectra Database (ver. 5.6.1), (online), available: https://physics.nist.gov/asd (May 25, 2020), National Institute of Standards and Technology, Gaithersburg, MD, 2019.
[47] K. A. Peterson and T. H. Dunning, Jr., J. Chem. Phys. **117**, 10548 (2002).
[48] B. P. Prascher, D. E. Woon, K. A. Peterson, T. H. Dunning, Jr., and A. K. Wilson, Theor. Chem. Acc. **128**, 69 (2011).
[49] The wave numbers of the $X^+\,^2\Sigma^+(v'' = 7) \leftarrow a\ ^3\Pi_0(v = 0)$ ionizing transitions of $^{24}MgAr$, $^{25}MgAr$, and $^{26}MgAr$ reported in Table 1 (third column) of Ref. 29 must be corrected from 39 341.1(5) cm^{-1}, 39 334.7(5) cm^{-1}, and 39 328.8(5) cm^{-1}, respectively, to 39 340.5(5) cm^{-1}, 39 334.1(5) cm^{-1}, and 39 328.2(5) cm^{-1}. All other table entries are not affected.
[50] G. Herzberg, *Molecular Spectra and Molecular Structure*, Spectra of Diatomic Molecules Vol. I, 2nd ed. (Van Nostrand Reinhold Company, New York, 1950).
[51] J. Thijssen, *Computational Physics*, 2nd ed. (Cambridge University Press, 2007).
[52] H. Hoshino, Y. Yamakita, K. Okutsu, Y. Suzuki, M. Saito, K. Koyasu, K. Ohshimo, and F. Misaizu, Chem. Phys. Lett. **630**, 111 (2015).
[53] C. Jonah, J. Chem. Phys. **55**, 1915 (1971).

[54]C. Pernot, J. Durup, J. B. Ozenne, J. A. Beswick, P. C. Cosby, and J. T. Moseley, J. Chem. Phys. **71**, 2387 (1979).
[55]R. N. Zare, *Angular Momentum* (John Wiley & Sons, New York, 1988).
[56]D. E. Manolopoulos and R. E. Wyatt, Chem. Phys. Lett. **152**, 23 (1988).
[57]T. N. Rescigno and C. W. McCurdy, Phys. Rev. A **62**, 032706 (2000).
[58]D. A. Telnov and S.-I. Chu, Phys. Rev. A **59**, 2864 (1999).
[59]S. Mukamel and J. Jortner, J. Chem. Phys. **61**, 5348 (1974).
[60]B. R. Cosofret, H. M. Lambert, and P. L. Houston, J. Chem. Phys. **117**, 8787 (2002).
[61]H. Kim, K. S. Dooley, S. W. North, G. E. Hall, and P. L. Houston, J. Chem. Phys. **125**, 133316 (2006).
[62]D. A. Varshalovich, A. N. Moskalev, and V. K. Khersonskii, in *Quantum Theory of Angular Momentum* (World Scientific, 1988), pp. 72–129.
[63]R. N. Zare, J. Chem. Phys. **40**, 1934 (1964).
[64]J. Tellinghuisen, "Photodissociation and photoionization," in *Advances in Chemical Physics*, edited by K. P. Lawley (John Wiley & Sons, 1985), Vol. LX, pp. 299–369.
[65]T. N. Rescigno and V. McKoy, Phys. Rev. A **12**, 522 (1975).